

# Torque Ripple Suppression of PMSM Using Fractional-Order Vector Resonant and Robust Internal Model Control

Mingfei Huang<sup>1</sup>, Yongting Deng<sup>1</sup>, *Member, IEEE*, Hongwen Li, *Member, IEEE*,  
and Jianli Wang<sup>2</sup>, *Member, IEEE*

**Abstract**—Periodic torque ripples caused by current harmonics seriously affect the control accuracy of the Permanent magnet synchronous motors (PMSMs). A conventional approach to reducing current harmonics is the use of a proportional–integral resonant controller in the current loop. Nonetheless, harmonics can still cause steady-state errors. Furthermore, the PI-based control structure is sensitive to parameter mismatches and uncertain disturbances, which will decrease the tracking performance of the current loop. To overcome the drawbacks of the traditional control method, a hybrid robust resonant control strategy was developed in this study. First, a vector resonant controller was enhanced by introducing fractional-order calculus (denoted as the fractional-order vector resonant (FOVR) controller in this article) so that it can suppress harmonic components more effectively. Then, a robust internal mode controller (Robust-IMC) was designed to improve the robustness and dynamic response and further reduce the current harmonics. Finally, by combining the FOVR controller and Robust-IMC, a control method—FOVR-Robust-IMC was designed as the robust control law to ensure satisfactory robustness and harmonics suppression performance. Meanwhile, the stability and robust stability of the developed control strategy were also analyzed. The results demonstrated that the proposed FOVR-Robust-IMC effectively reduced the harmonic components and improved the robustness to parameter mismatch.

**Index Terms**—Fractional-order vector resonant (FOVR) controller, harmonics suppression, permanent magnet synchronous motor (PMSM), robust internal mode control.

## I. INTRODUCTION

PERMANENT magnet synchronous motors (PMSMs) offer high efficiency, a fast response, and low electrical loss. Thus, they are widely applied in industrial drive systems, such as electric vehicles and large-scale systems [1]–[5]. However, nonideal factors (e.g., parameter mismatches, current measurement errors, and dead-time effects of the inverter)

Manuscript received October 18, 2020; revised January 4, 2021; accepted January 16, 2021. Date of publication January 20, 2021; date of current version August 24, 2021. This work was supported in part by the National Natural Science Foundation of China under Grant 11603024 and Grant 11973041 and in part by the Youth Innovation Promotion Association, Chinese Academy of Sciences (CAS), under Grant 2019218. (*Corresponding authors: Yongting Deng; Hongwen Li.*)

Mingfei Huang is with the Changchun Institute of Optics, Fine Mechanics, and Physics, Chinese Academy of Sciences, Changchun 130033, China, and also with the University of Chinese Academy of Sciences, Beijing 100049, China (e-mail: ciomphmf@163.com).

Yongting Deng, Hongwen Li, and Jianli Wang are with the Changchun Institute of Optics, Fine Mechanics, and Physics, Chinese Academy of Sciences, Changchun 130033, China (e-mail: dyt0612@163.com; lihongwen@ciomp.ac.cn; wangjianli@ciomp.ac.cn).

Digital Object Identifier 10.1109/TTE.2021.3053063

cause the stator current to contain harmonic components that result in torque ripples [6]–[8]. These torque ripples result in periodic oscillations in the speed steady state, which reduces the accuracy of the servo control system [9].

Several methodologies have been employed to attenuate current harmonics. They can be grouped into two approaches. In the first approach, the key dimensional parameters of the motor are optimized to suppress current harmonics [10]–[12]. Although improving the structure is an effective approach, this complicates the motor structure and increases the manufacturing costs. The second approach is to use control algorithms to modify the input current or voltage. This has the advantages of requiring no additional hardware and being easily introduced to motor machines. Therefore, this article focuses on employing control algorithms to suppress current harmonics.

Numerous control methods have been proposed to compensate for current harmonics. Iterative learning control was utilized to reduce current harmonics and torque ripples in [2], [9], and [13]; however, this algorithm depends on specific states and needs a certain amount of data storage. To compensate for periodic disturbances, the repetitive controller has been utilized in a current loop to achieve zero static error tracking of periodic components in the reference current [14]–[16]. Despite its advantages, this control scheme requires a long time interval to reach steady-state conditions. Wu *et al.* [17] developed a comprehensive disturbance observer to estimate the torque ripples caused by multiple disturbance sources. This observer-based technology can achieve satisfactory minimizing effects on current harmonics although nonlinear factors are not considered. Yan *et al.* [18] proposed a torque ripple suppression method by introducing two decoupled PI regulators, and the speed ripple caused by current harmonics was obviously reduced.

An alternative harmonics suppression control strategy is to employ resonant controllers that have high computational efficiency and flexibility. This control strategy is thus widely used in pulsewidth-modulated rectifiers [15] and parallel inverters [19]. Husev *et al.* [20] reported numerous conventional resonant controllers. Among them, the ideal resonant controller and quasi-resonant controller are the most typical and widely used [21], [22].

The ideal resonant controller can achieve zero static error tracking of periodic components. However, it is sensitive to frequency variations and may destabilize the system in the case of a significant computational delay. To increase the stability,

some researchers have suggested using a quasi-resonant (R) controller with a damping term. Applying a cutoff frequency increases stability; it results in a large steady-state error [20]. In [23], a vector controller (VR) is proposed by introducing inductance and resistance parameters to decrease the steady-state error and cancel the phase delay caused by the control plant. However, the parameter mismatch will affect the amplitude–phase characteristics of the VR controller, which may decrease the harmonics suppression performance. In view of this problem, the fractional-order vector resonant (FOVR) controller was designed in this study. The modified FOVR controller takes advantage of the properties of the VR controller and fractional calculus [24]–[27], thereby further improving the harmonics suppression performance.

A control structure using several resonant controllers (Rs or VRs) paralleled with a PI controller is conventionally adopted to regulate the current and compensate for the current harmonics [28], [29]. However, the traditional PI controller is sensitive to parameter mismatching, which will decrease the tracking accuracy of the current loop [30]. Thus, robust performance should be considered in the current controller design.

The sliding mode control and disturbance observer [9], [30] are effective methods to solve the negative effects of parameter mismatching and uncertain disturbances; however, they have some drawbacks; i.e., the inherent chattering caused by the switch function may excite the high-frequency unmodeled dynamics, and the upper bound of the uncertain disturbance is difficult to determine. The robust internal mode controller (Robust-IMC) provides a practical solution to improving the robustness of the control system, due to its simple implementation, providing the desired dynamic response and a low dynamic order [31]. This control strategy is widely applied in the electric drive field [31]–[33]. Therefore, this study adopts the Robust-IMC as an auxiliary controller to attenuate the disturbance and improve the robustness to parameter mismatching of the current loop.

Consequently, this article develops a new control method named FOVR-Robust-IMC by combining the FOVR controller and the Robust-IMC to enhance the performance of harmonics suppression. The constituent FOVR controller is designed to ensure that the VR controller maintains sufficient resonant gain and further improves the harmonics suppression performance in the parameter mismatch case. Meanwhile, the constituent Robust-IMC is incorporated to improve the robustness of the current loop and obtain the desired dynamic behavior. Furthermore, the distinct features of stability and robust stability of the proposed FOVR-Robust-IMC are analyzed by the small gain theorem. Finally, simulations and experiments are conducted to verify that the phase current waveform,  $d$ – $q$ -axis tracking trajectory, and speed steady-state performance are improved when the FOVR-Robust-IMC is applied in a PMSM drive system.

The remainder of this article is organized as follows. Section II describes the overall dynamic model of a PMSM, presents an analysis of the PMSM torque ripples caused by current harmonics, and provides a definition of fractional calculus. Section III demonstrates the design process

and performance analysis of the explored control method. Section IV presents the simulations and experiments that were performed to verify the servo control performance of the proposed algorithm. Finally, our main conclusions are presented in Section V.

## II. DYNAMIC MODEL OF A PMSM AND FRACTIONAL-ORDER SYSTEM

### A. Dynamic Model of a PMSM

The dynamic model of a PMSM on the  $d$ – $q$ -axis is given by

$$\begin{cases} u_d = Ri_d + L_d \frac{di_d}{dt} - \omega_h L_q i_q \\ u_q = Ri_q + L_q \frac{di_q}{dt} + \omega_h L_d i_d + \omega_h \psi_f \end{cases} \quad (1)$$

where  $u_d, u_q, i_d, i_q, L_d$ , and  $L_q$  are the stator voltages, stator currents along  $d$ - and  $q$ -axes, and  $d$ – $q$  frame inductances, respectively. A surface-mounted PMSM is considered, and  $L_d$  and  $L_q$  satisfy  $L_d = L_q$ . Meanwhile,  $R$  is the resistance of the PMSM,  $\omega_h$  denotes the electrical angular speed, and  $\psi_f$  is the PM flux linkage.

The dynamic model of a PMSM under a mechanical load is given by

$$J \dot{\omega}_m = T_e - T_L - B \omega_m \quad (2)$$

where  $\omega_m, T_e, T_L, B$ , and  $J$  represent the mechanical angular speed, electromagnetic torque, load torque, frictional coefficient, and inertial constant, respectively.

When field-oriented control is utilized for a PMSM, the maximum output torque can be obtained by maintaining the  $d$ -axis current at zero. Then, the control input for the electromagnetic torque equation can be described as

$$T_e = 1.5 p \psi_f i_q = K_t i_q \quad (3)$$

where  $p$  is the pole pair and  $K_t$  is the torque constant.

### B. Torque Ripple Analysis

The sources of the torque ripple caused by the PMSM can be divided into two main types: those caused by cogging torque and those caused by harmonic torque. The cogging torque is mainly produced by the mutual effect of magnetic flux and stator slots. To date, no accurate model exists for describing the cogging torque. Therefore, using a mathematical method to compensate for this torque is difficult. The harmonic torque is another important part of the torque ripple produced by the parameter mismatch, current measurement errors, and dead time effects of the inverter [28]. When the fundamental components of the electromotive force and stator current are in the same phase, the electromagnetic torque can be expressed as

$$\begin{aligned} T_e(t) &= \frac{1}{\omega_m} (e_a(t)i_a(t) + e_b(t)i_b(t) + e_c(t)i_c(t)) \\ &= T_0 + T_6 \cos(6\omega_h t) + T_{12} \cos(12\omega_h t) \\ &= T_0 + T_{\text{harmonic}} \end{aligned} \quad (4)$$

$$\begin{cases} T_0 = \frac{3}{2\omega_m} [E_{m1}I_{m1} + E_{m5}I_{m5} + E_{m7}I_{m7} + \dots] \\ T_6 = \frac{3}{2\omega_m} [(E_{m7} - E_{m5})I_{m1} + (E_{m11} - E_{m1})I_{m5} \\ + (E_{m13} - E_{m1})I_{m7} + \dots] \\ T_{12} = \frac{3}{2\omega_m} [(E_{m13} - E_{m11})I_{m1} + (E_{m17} - E_{m7})I_{m5} \\ + (E_{m19} - E_{m5})I_{m7} + \dots] \end{cases} \quad (5)$$

where  $T_0$ ,  $T_6$ , and  $T_{12}$  are the average electromagnetic torque, sixth-harmonic torque, and 12th-harmonic torque, respectively; and  $T_{\text{harmonic}}$  is the total harmonic torque. The mechanical angular speed  $\omega_m$  and the electrical angular speed  $\omega_h$  satisfy  $\omega_h = p\omega_m$ .  $E_{m1}$  is the fundamental electromotive force.  $E_{m5}$ ,  $E_{m7}$ ,  $E_{m11}$ ,  $E_{m13}$ ,  $E_{m17}$ , and  $E_{m19}$  are the fifth-, seventh-, 11th-, 13th-, 17th-, and 19th-harmonic components, respectively.  $I_{m1}$  is the fundamental component of the stator current.  $I_{m5}$ ,  $I_{m7}$ , and  $I_{m11}$  are the fifth-, seventh-, and 11th-harmonic components, respectively, of the stator current. According to (5),  $T_0$  is produced by the interaction between the stator current and the electromotive force with the same order,  $T_{\text{harmonic}}$  is caused by different orders for the stator current and electromotive force, and the sixth-harmonic torque is the dominant component [28].

According to (2), (4), and (5), the transfer function between the electrical angular speed and electromagnetic torque can be expressed as

$$\omega_m(s) = \frac{T_0(s) + T_{\text{harmonic}}(s) - T_L(s)}{Js + B}. \quad (6)$$

According to (6), the harmonic torque will result in the same frequency as the harmonic speed component, and the sixth-harmonic torque is the dominant component. Therefore, the proposed controller suppresses the sixth-harmonic torque component on the  $d$ - $q$ -axis.

### C. Fractional-Order System Preliminaries

First, some basic notations and definitions for fractional-order operators are given. Fractional calculus is an extension of the integer order. The continuous fractional-order integral-differential operator is given as

$${}_a D_t^\xi = \begin{cases} \frac{d^\xi}{dt^\xi}, & \xi > 0 \\ 1, & \xi = 0 \\ \int_a^t (dt)^{-\xi}, & \xi < 0 \end{cases} \quad (7)$$

where  $D$  is the fractional operator,  $\xi$  is the fractional-order  $\xi \in \mathfrak{R}$ , and  $a$  and  $t$  are the operator limits. The three most important and frequently used definitions for fractional-order systems are the Caputo, Grunwald-Letnikov (GL), and Riemann-Liouville (RL) definitions. The  $x$ th Caputo definition can be described as

$${}_a D_t^\xi g(t) = \frac{1}{\Gamma(n - \xi)} \int_a^t \frac{g^n(t)}{(t - \tau)^{\xi+1-n}} dt, \quad n-1 < \xi < n \quad (8)$$

where  $\Gamma(\cdot)$  represents the gamma function, which can be expressed as

$$\Gamma(z) = \int_0^\infty e^{-t} t^{z-1} dt. \quad (9)$$

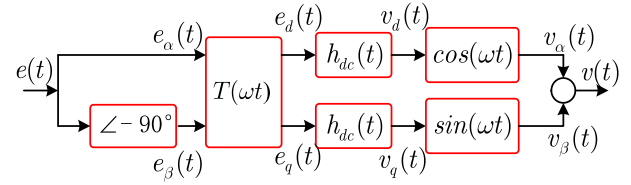


Fig. 1. Block diagram of demodulating and modulating a single-phase integral block.

In contrast to the Caputo definition, the  $x$ th-order GL definition for an arbitrary order is given as

$${}_a D_t^\xi g(t) = \frac{1}{\Delta^\xi} \sum_{j=0}^k (-1)^j \binom{\xi}{j} g(k-j) \quad (10)$$

where  $\Delta$  is the sampling interval and  $k$  is the number of samples.  $\binom{\xi}{j}$  denotes the binomial coefficients, which can be calculated as

$$\binom{\xi}{j} = \begin{cases} 1, & j = 0 \\ \frac{\xi(\xi-1)\dots(\xi-j+1)}{j!}, & j = 1, 2, 3, \dots \end{cases} \quad (11)$$

The  $\xi$ th-order RL definition is given as

$${}_a D_t^\xi g(t) = \frac{1}{\Gamma(l - \xi)} \frac{d^l}{dt^l} \int_a^t \frac{g(\tau)}{(t - \tau)^{\xi+1-l}} dt \quad (12)$$

where  $l$  is the first integer that satisfies  $l - 1 \leq \xi < l$ .

The Laplace transform is a routine integral transform method that is commonly used in engineering technology. This method is also suitable for fractional-order systems. According to (12), the Laplace transform of the RL fractional derivative can be expressed as

$$L\{{}_0 D_t^{\pm\xi} g(t)\} = \int_0^\infty e^{-st} {}_0 D_t^{\pm\xi} g(t) = s^{\pm\xi} L\{g(t)\} \quad (13)$$

where  $s \equiv j\omega$  is the transform variable.

## III. DESIGN OF THE FOVR-ROBUST-IMC

A resonant controller is a generalized integrator in a stationary frame. The three kinds of traditional resonant controllers are briefly described here to highlight their main advantages and shortcomings. These shortcomings motivated the design of the proposed FOVR controller, which is detailed later in this section. Then, the FOVR-Robust-IMC is proposed by further incorporating the Robust-IMC to suppress the torque ripples produced by current harmonics.

### A. Review of Resonant Controllers

Fig. 1 shows a current control diagram in a stationary frame with a synchronous rotation axis [33], where  $e(t)$  is the current error.  $e_\alpha(t)$  and  $e_\beta(t)$  represent the current error in the  $a$ - $b$ -axis.  $e_\beta(t)$  lags  $e_\alpha(t)$   $-90^\circ$  in the phase after a delay.  $T(\omega t)$  is the Park transformation matrix.  $e_d(t)$  and  $e_q(t)$  denote the current error on the  $d$ - $q$ -axis.  $v_d(t)$  and  $v_q(t)$  are the outputs of the controller  $h_{dc}(t)$  in the synchronous frame.  $v_\alpha(t)$

and  $v_\beta(t)$  are the control commands in the station frame.  $v(t)$  is the final control result.

The Park transformation matrix can be expressed as

$$T(\omega t) = \begin{bmatrix} \cos(\omega t) & \sin(\omega t) \\ -\sin(\omega t) & \cos(\omega t) \end{bmatrix}. \quad (14)$$

According to Fig. 1,  $e_d(t)$  and  $e_q(t)$  can be deduced as

$$\begin{cases} e_d(t) = e_\alpha(t) \cos(\omega t) + e_\beta(t) \sin(\omega t) \\ e_q(t) = -e_\alpha(t) \sin(\omega t) + e_\beta(t) \cos(\omega t). \end{cases} \quad (15)$$

Then,  $v_d(t)$  and  $v_q(t)$  can be given as

$$\begin{cases} v_d(t) = e_d(t) \otimes h_{dc}(t) \\ v_q(t) = e_q(t) \otimes h_{dc}(t) \end{cases} \quad (16)$$

where  $\otimes$  is the convolution operator.

Using the results for  $v_d(t)$  and  $v_q(t)$ , the output  $v(t)$  can be represented as

$$v(t) = v_d(t) \cos(\omega t) - v_q(t) \sin(\omega t). \quad (17)$$

Combining (15)–(17),  $v(t)$  can be rewritten as

$$v(t) = h_{dc}(t) \otimes [(e_d(t) \cos(\omega t) + e_\beta(t) \sin(\omega t)) \cos(\omega t) - h_{dc}(t) \otimes [(e_d(t) \sin(\omega t) + e_\beta(t) \cos(\omega t)) \sin(\omega t)]. \quad (18)$$

Based on the Laplace transform and mathematical derivation, the control output of  $V(s)$  can be expressed as

$$V(s) = V_\alpha(s) + V_\beta(s) \quad (19)$$

where

$$V_\alpha(s) = \frac{1}{2} [H(s - j\omega)E_\alpha(t) + H(s + j\omega)E_\alpha(t)] \quad (20)$$

and  $V(s)$ ,  $V_\alpha(s)$ ,  $V_\beta(s)$ ,  $E_\alpha(s)$ , and  $H(s)$  represent the Laplace transform of  $v(t)$ ,  $v_\alpha(t)$ ,  $v_\beta(t)$ ,  $e_\alpha(t)$ , and  $h_{dc}(t)$ , respectively.  $V_\beta(s)$  has a phase lag of  $-90^\circ$  with respect to  $V_\alpha(s)$ .

According to (20), the regulation performances of the dc regulator in the synchronous and stationary frames are identical. They have the same frequency response characteristics in the bandwidth of concern. For ideal integrators with  $H_{ac1}(s) = k_r/s$ , where  $k_r$  is the gain regulation parameter, the ideal resonant controller is given as

$$H_{ac1}(s) = \left( \frac{k_r}{s + j\omega_0} - \frac{k_r}{s - j\omega_0} \right) = \frac{2k_r s}{s^2 + \omega_0^2}. \quad (21)$$

It can be described as

$$\begin{cases} |H_{ac1}(j\omega)| = \begin{cases} \infty, & \omega = \omega_0 \\ 0, & \text{else} \end{cases} \\ \angle |H_{ac1}(j\omega)| = \begin{cases} 90^\circ, & 0 \leq \omega < \omega_0 \\ -90^\circ, & \omega > \omega_0 \end{cases} \end{cases} \quad (22)$$

where  $\omega_0$  is the resonant frequency.

According to (22), the ideal resonant controller has infinite gain at the resonant frequency and can achieve a zero tracking error for the ac signal. However, it has a narrow bandwidth. It is, thus, sensitive to frequency variations. In addition, an infinite gain increases the word length in the case of digital implementation and destabilizes an open loop. To avoid these

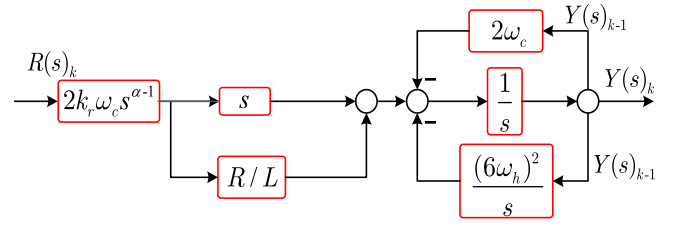


Fig. 2. Implementation of the digital FOVR controller.

problems, the ideal integrator can be replaced with a nonideal integrator  $H_{dc2}(s) = k_r/(1 + s/\omega_c)$ , where  $\omega_c$  is the damping frequency that satisfies  $\omega \gg \omega_c$ . The R controller is then represented as follows:

$$H_{ac2}(s) = \frac{k_r}{1 + \frac{s}{\omega_c} + \frac{j\omega_0}{\omega_c}} + \frac{k_r}{1 + \frac{s}{\omega_c} - \frac{j\omega_0}{\omega_c}} \approx \frac{2k_r\omega_c s}{s^2 + 2\omega_c s + \omega_0^2} \quad (23)$$

with

$$|H_{ac2}(j\omega)| = k_r/\omega_c, \quad |\angle H_{ac2}(j\omega)|(\omega \rightarrow \omega_0)^\pm < 90^\circ. \quad (24)$$

The R controller appears flawless in terms of the damping cutoff frequency, which expands the stability domain while maintaining a high resonant gain. However, it increases the steady-state error [20]. To improve the resonant gain and reduce the phase delay caused by the control plant, a VR controller is proposed in [15] and [23], which is expressed as follows:

$$G(s)_{\text{IOVR}} = \frac{2k_r\omega_c s(s + R/L)}{s^2 + 2\omega_c s + \omega^2}. \quad (25)$$

The VR controller has a second-order term in the molecules by embedding the inverse of the control plant. However, the parameter mismatch may reduce the resonant gain and affect the harmonics suppression performance.

### B. Proposed FOVR Controller

Based on the analysis in Section III-A, a fractional-order term is added in the molecules of the vector resonant controller, which results in the following optimized transfer function:

$$G(s)_{\text{FOVR}} = \frac{2k_r\omega_c s^\alpha (s + R/L)}{s^2 + 2\omega_c s + \omega^2} \quad (26)$$

where  $\alpha$  denotes the fractional exponent and should be selected in the range of  $[1, 2)$  [24]. Based on (26), the proposed resonant controller can be rewritten as

$$Y(s)_k = \frac{-2\omega_c}{s} Y(s)_{k-1} - \frac{(6\omega_h)^2}{s^2} Y(s)_{k-1} + R(s)_k \frac{2k_r\omega_c s^\alpha (s + R/L)}{s^2} \quad (27)$$

where  $Y(s)_k$  and  $R(s)_k$  are the  $k$ th control output and input of the FOVR controller, respectively. As shown in (27), three terms contain an integral part  $1/s$ ; thus, the FOVR controller can be described by the diagram shown in Fig. 2.

To illustrate the influence of  $k_r$ ,  $\omega_c$ , and  $\alpha$  on the FOVR controller, a simulation experiment is carried out with varying parameters at a center frequency  $\omega = 400 \pi$  rad/s.

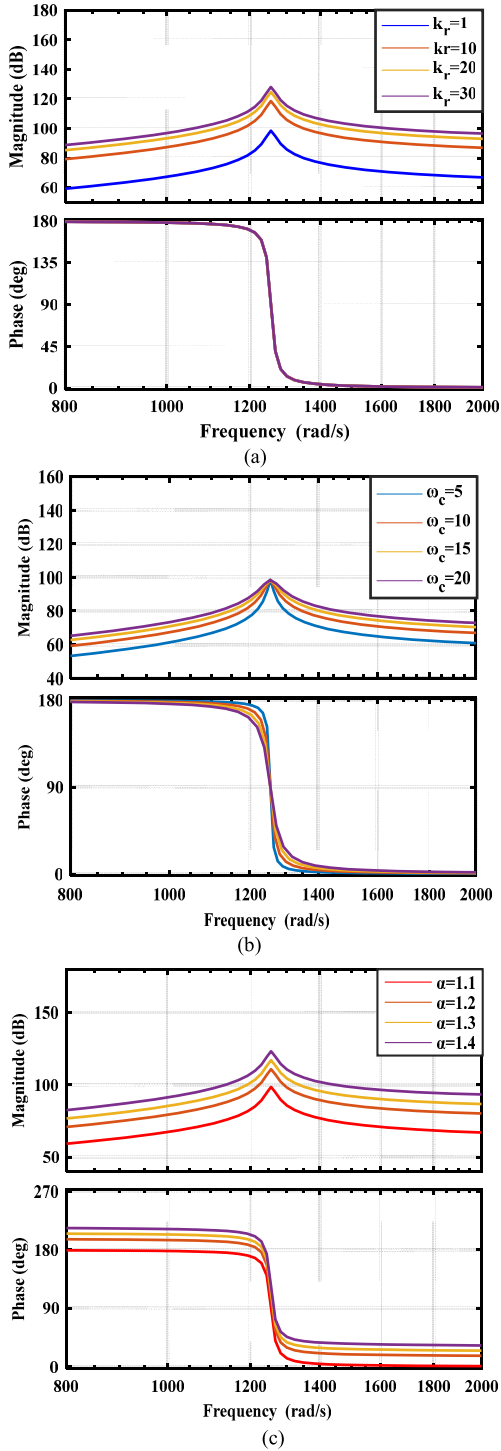


Fig. 3. Amplitude–phase characteristics of the FOVR controller: (a) increasing  $k_r$  with constant  $\omega_c = 10$  rad/s and  $\alpha = 1$ , (b) increasing  $\omega_c$  with constant  $k_r = 10$  and  $\alpha = 1$ , and (c) increasing  $\alpha$  with constant  $k_r = 10$  and  $\omega_c = 10$  rad/s.

Fig. 3(a) shows the Bode diagrams of  $G(s)_{\text{FOVR}}$  with varying  $k_r$  and fixed  $\omega_c = 10$  rad/s and  $\alpha = 1$ . It can be observed that the peak gain of the FOVR controller is proportional to  $k_r$ . A larger  $k_r$  increases the gain, which improves the harmonics suppression. However, the bandwidth shows the minimal change.

Fig. 3(b) shows the amplitude–frequency characteristics of the FOVR controller with varying  $\omega_c$  when  $k_r = 10$  and  $\alpha = 1$ .

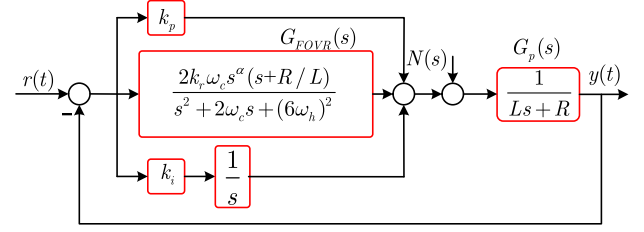


Fig. 4. Current control diagram of the PI-FOVR controller.

It shows that reducing  $\omega_c$  increases the gain but decreases the bandwidth. This results in poor robustness to frequency variations. In practical controller design,  $\omega_c$  values of 5~15 rad/s have been found to obtain a satisfactory balance [32].

Fig. 3(c) illustrates the impact of the order  $\alpha$  on the FOVR controller when  $k_r = 10$  rad/s and  $\omega_c = 10$  rad/s. It can be observed that a large  $\alpha$  results in large peak gain; however, the bandwidth remains fixed. Meanwhile, the frequency response curve shifts above  $0^\circ$ , which indicates that the phase margin will be improved in an open loop. Therefore,  $\alpha$  can be regarded as a parameter that can tune the resonant gain and phase margin of the FOVR controller.

Analysis of the tuning parameters  $k_r$ ,  $\omega_c$ , and  $\alpha$  shows that the peak gain, bandwidth, and phase margin are regulated more smoothly with the proposed controller than with the traditional VR controller. In addition, increasing the order increases the degrees of freedom of the VR controller, which may improve the harmonics suppression performance.

### C. Design of the PI-FOVR Controller

In this section, the PI controller is designed to obtain a gain crossover frequency of 250 Hz and a phase margin of  $103^\circ$  in an open loop (i.e.,  $k_p = 0.3$  and  $k_i = 10$ ). Thus, the PI-FOVR controller can be expressed as

$$G(s)_{\text{PI-FOVR}} = C(s) + G(s)_{\text{FOVR}} \quad (28)$$

where  $C(s) = k_p + k_i/s$ , and  $G(s)_{\text{FOVR}} = \frac{2k_r\omega_c s^\alpha (s+R/L)}{s^2+2\omega_c s+(6\omega_h)^2}$ .

Fig. 4 shows the current control diagram with the PI-FOVR controller. To reduce current harmonics, the gain of  $C(s)$  and  $G(s)_{\text{FOVR}}$  should be maximized in the frequency band of interest. With the proposed control method, the transfer function of the current loop is expressed as

$$Y(s) = \frac{(G_{\text{FOVR}}(s) + C(s))G_p(s)}{1 + (G_{\text{FOVR}}(s) + C(s))G_p(s)}R(s) + \frac{(N(s))G_p(s)}{1 + (G_{\text{FOVR}}(s) + C(s))G_p(s)} \quad (29)$$

where  $N(s)$  represents the sixth-harmonic disturbance.  $G_p(s)$  is the control plant of the current loop, which is simplified to  $1/(Ls + R)$  [27].

To analyze the effect of  $G(s)_{\text{FOVR}}$  on the performance of the PI-FOVR controller, the steady-state error between the command and output is defined as

$$\Delta i(s) = Y(s) - R(s) = E_1(s) + E_2(s) \quad (30)$$

where  $E_1(s) = R(s)/T(s)$ ,  $E_2(s) = N(s)G_p(s)/T(s)$ , and  $T(s) = 1 + (G_{\text{FOVR}}(s) + C(s))G_p(s)$ .

The steady-state error is divided into two parts:  $E_1(s)$  due to system structure and input signals, and  $E_2(s)$  due to disturbances of the high-frequency current harmonics. When  $6\omega_h \gg \omega$  and  $C(\omega) \gg G(j\omega)_{\text{FOVR}}$ , then  $T(s) = 1 + C(s)G_p(s)$  and  $E_1(s)$  can be expressed as

$$E_1(s) = \frac{R(s)s}{s + k_p(s + k_i)G_p(s)}. \quad (31)$$

The following error can be easily minimized by setting a large integral constant  $k_i$ . According to the final-value theorem, this will converge to zero. Therefore, we focused on the steady-state error caused by harmonics disturbance.

When  $\omega$  approaches  $6\omega_h$ ,  $G(j\omega)_{\text{FOVR}} \gg C(\omega)$  and  $T(s)$  becomes  $T(s) = 1 + G_p(s)G_{\text{FOVR}}(s)$ .

Note that

$$|s^\alpha(j\omega)|_{\omega_h} = \frac{\omega_h^\alpha \sqrt{\sin(\alpha\pi)^2 + (1 - \cos(\alpha\pi))^2}}{2} = \omega_h^\alpha. \quad (32)$$

Then,  $E_2(s)$  can be represented as

$$E_2(s)_{\text{PI-FOVR}} \approx \frac{(6\omega_h - \omega_c)N(j6\omega_h)G_p(j6\omega_h)}{6\omega_h(\omega_h^\alpha + 1)k_r}. \quad (33)$$

According to (33), the steady-state error is inversely proportional to  $\omega_h^\alpha$  and  $k_r$ . A larger  $\alpha$  and  $k_r$  result in smaller steady-state error. However, the influence of the two parameters on the steady-state error is quite different. The fraction order term  $\alpha$  makes the term  $E_2(s)_{\text{PI-FOVR}}$  decrease exponentially, while  $k_r^{-1}$  makes  $E_2(s)_{\text{PI-FOVR}}$  decrease linearly. Thus, it is obviously the case that  $E_2(s)_{\text{PI-FOVR}}$  is more sensitive to  $\alpha$  tuning than to  $k_r$  tuning.

Consider the current loop with the R controller in (23). The steady-state error  $E_2(s)_{\text{PI-R}}$  is expressed as

$$E_2(s)_{\text{PI-R}} \approx \frac{(6\omega_h - \omega_c)}{6\omega_h k_r} N(j6\omega_h)G_p(j6\omega_h). \quad (34)$$

According to (33) and (34), the relationship between the state errors  $E_2(s)_{\text{PI-FOVR}}$  and  $E_2(s)_{\text{PI-R}}$  can be expressed as

$$E_2(s)_{\text{PI-FOVR}} \approx \frac{E_2(s)_{\text{PI-R}}}{(\omega_h^\alpha + 1)}. \quad (35)$$

Based on (35), it can be observed that the VR controller ( $\alpha = 1$ ) and FOVR can further reduce the steady-state error caused by harmonics. In addition, the FOVR controller has more degrees of freedom in parameter tuning, which can attenuate the harmonics more effectively.

The open-loop Bode diagrams of the PI controller with the R, VR, and FOVR controllers are conducted to validate the performance of the proposed FOVR controller. The parameters employed in the simulation are set as follows:  $L = 0.0085$  H,  $R = 0.569$   $\Omega$ ,  $k_r = 1$ ,  $\omega_c = 10$  rad/s, and  $\alpha = 1.2$ . If the electrical angular frequency  $\omega_h$  is set as  $\omega_h = 100$  rad/s, then the resonant frequency  $\omega_{6h} = 600$  rad/s can be determined.

It can be observed from Fig. 5 that the resonant gain with R controller is 12.4 dB, while that with VR and FOVR are 72.6 and 83.4 dB, respectively. Furthermore, the phase margins with R, VR, and FOVR are 49.4°, 91°, and 101°, respectively. Note that phase margin determines the damping ratio [34]. This simulation shows that the FOVR controller can provide better harmonics suppression performance compared with the R and VR controllers.

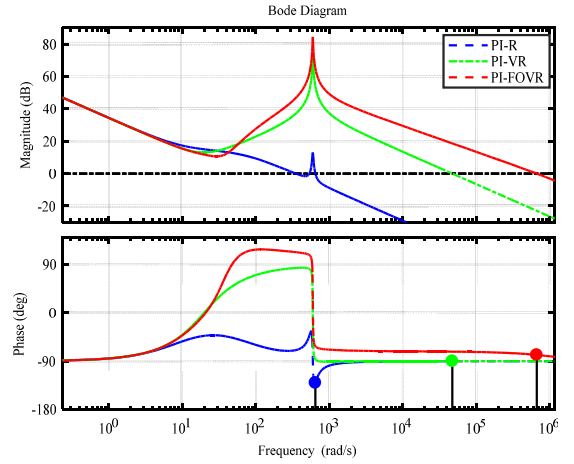


Fig. 5. Current loop amplitude-phase characteristics of three resonant controllers.

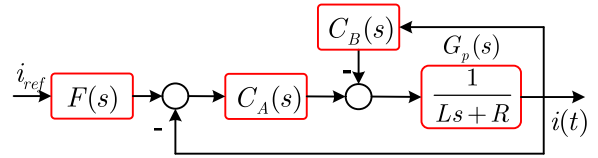


Fig. 6. Diagram of Robust-IMC.

#### D. Design of the Robust-IMC Controller

The Robust-IMC strategy utilizes the controlled plant model as an explicit part of the controller parameters, which has the advantages of simplicity and robustness with respect to parameter mismatching, and it provides the desired transition response [31], [35], [36]. Hence, the Robust-IMC is adopted as an auxiliary controller to replace the PI controller. Fig. 6 shows a diagram of robust Robust-IMC.  $F(s)$ ,  $C_A(s)$ , and  $C_B(s)$  are the components of the Robust-IMC to be designed, which will be detailed later.

According to [35], the IMC filter is given as

$$f(s) = \frac{2\lambda s + 1}{s^2 + 2\lambda s + 1} \quad (36)$$

where  $\lambda$  is a time constant of the filter determining robust performance with respect to parameter mismatching and uncertainty.

Based on the internal model control principle presented in [31], the Robust-IMC can be obtained as follows:

$$C_A(s) = \frac{G_{ry}(s)}{(1 - G_{ry}(s))} \frac{(L_n s + R_n)}{1 - f(s)} \quad (37)$$

$$F(s) = \frac{f_D(s)}{f(s)} \quad (38)$$

$$C_B(s) = \frac{(L_n s + R_n)f(s)}{1 - f(s)} = \frac{2\lambda L_n}{s^2} \left( s + \frac{1}{2\lambda} \right) \left( s + \frac{R_n}{L_n} \right) \quad (39)$$

where  $L_n$  and  $R_n$  are the parameters of the nominal model of the current loop, which can be determined by prior knowledge and experience.  $f_D(s)$  is a low-pass filter that is used to improve the tracking performance.  $G_{ry}(s)$  is the desired

transition response, which can be expressed as

$$G_{ry}(s) = \frac{1}{\tau s + 1} \quad (40)$$

where  $\tau$  is the time constant of  $G_{ry}(s)$ . When uncertainty and disturbance are considered, the real dynamic response  $G_{ry}(s)'$  can be represented as follows:

$$G_{ry}(s)' = (1 + (1 - f(s))\Delta G_p(s))G_{ry}(s) + (1 - f(s))(1 - G_{ry}(s))d(s) \quad (41)$$

where  $\Delta G_p(s)$  and  $d(s)$  denote the respective model uncertainty and disturbance.

To obtain satisfactory robust performance,  $\tau$  should be chosen such that  $\tau \gg \lambda$  [30]. Then, the high pass filter  $(1 - f(s))$  maintains negative gain in the frequency domain within the bandwidth of  $G_{ry}(s)$ . It is not difficult to verify that  $(1 - f(s))(\Delta G_p(s) + d(s))$  is closed to zero. Therefore, the Robust-IMC can still ensure satisfactory robustness when the uncertainty disturbance occurs.

Based on (36), (37), and (40),  $C_A(s)$  can be deduced as

$$C_A(s) = \frac{(s^2 + 2\lambda s + 1)(L_n s + R_n)}{\tau s^3}. \quad (42)$$

In order to improve the tracking performance of the current loop, the filter  $f_D(s)$  is chosen as follows:

$$f_D(s) = \frac{\lambda s + 1}{s^2 + 2\lambda s + 1}. \quad (43)$$

According to (36) and (43), the setting filter  $F(s)$  is derived as

$$F(s) = \frac{\lambda s + 1}{2\lambda s + 1}. \quad (44)$$

Combining (39), (42), and (44) and using the inverse Laplace transform, the Robust-IMC can be written as follows:

$$\begin{aligned} u_{\text{IMC}} = & k_{pe}e(t) + k_{ie1} \int_0^t e(t)dt + k_{ie2} \int_0^t \int_0^t e(t)dt \\ & + k_{ie3} \int_0^t \int_0^t \int_0^t e(t)dt - k_{py}i(t) \\ & - k_{iy1} \int_0^t i(t)dt - k_{iy2} \int_0^t \int_0^t i(t)dt \end{aligned} \quad (45)$$

where  $e(t) = i_{\text{ref}}F(s) - i(t)$ ,  $k_{pe} = (L_n/\lambda)$ ,  $k_{ie1} = (L_n/\tau)((2/\lambda) + (R_n/L_n))$ ,  $k_{ie2} = (L_n/\tau)((1/\lambda^2) + (2R_n/L_n\lambda))$ ,  $k_{ie3} = (R_n/\tau\lambda^2)$ ,  $k_{py} = (2L_n/\lambda)$ ,  $k_{iy1} = L_n((1/\lambda^2) + (2R_n/L_n\lambda))$ , and  $k_{iy2} = (R_n/\lambda^2)$ .

Here,  $i_{\text{ref}}$  is the command current, and  $i(t)$  represents the feedback. As can be observed from (44),  $F(s)$  is a low-pass filter; hence,  $i_{\text{ref}}F(s)$  will asymptotically converge to  $i_{\text{ref}}$ , and  $e(t)$  can be considered as

$$e(t) = i_{\text{ref}} - i(t). \quad (46)$$

As can be observed in (45), the Robust-IMC is a controller with a number of integral links. To avoid iterated integral

overflow, the following state variables are defined:

$$\begin{aligned} x_1 = e(t), x_2 = & \int_0^t e(t)dt - \frac{i_{\text{ref}}\alpha_1 k_{pe}}{(k_{ie1} + k_{iy1})} \\ x_3 = & \int_0^t \left[ \int_0^r e(\delta)d\delta - \frac{i_{\text{ref}}\gamma_1 k_{iy1}}{k_{ie2} + k_{iy2}} \right] dr - \frac{i_{\text{ref}}\alpha_2 k_{py}}{(k_{ie2} + k_{iy2})} \\ x_4 = & \int_0^t \left\{ \int_0^r \left[ \int_0^d e(\theta)d\theta - i_{\text{ref}} \frac{k_{iy2}}{k_{ie3}} \right] \right. \\ & \left. d\delta - i_{\text{ref}} \frac{\gamma_2 k_{iy1}}{k_{ie3}} i_{\text{ref}} \right\} dr - \frac{R i_{\text{ref}}}{k_{ie3}} - \frac{\alpha_3 i_{\text{ref}} k_{py}}{k_{ie3}} \end{aligned}$$

where  $\alpha_1, \gamma_1 \in \mathfrak{R}^+$ ,  $\alpha_2, \alpha_3, \gamma_2 \in \mathfrak{R}$ . If  $\alpha_1, \alpha_2, \alpha_3, \gamma_1$ , and  $\gamma_2$  satisfy the following condition:

$$\begin{cases} \alpha_1 + \alpha_2 + \alpha_3 = 1 \\ \gamma_1 + \gamma_2 = 1 \\ \frac{\alpha_1 k_{pe}}{k_{ie1} + k_{iy1}} = \frac{k_{iy2}}{k_{ie3}} = \frac{\gamma_1 k_{iy1}}{k_{ie2} + k_{iy2}} \\ \frac{\alpha_2 k_{py}}{(k_{ie2} + k_{iy2})} = \frac{\gamma_2 k_{iy1}}{k_{ie3}} \end{cases}. \quad (47)$$

We can write

$$\dot{x}_4 = x_3, \dot{x}_3 = x_2, \dot{x}_2 = x_1. \quad (48)$$

Then, the control law in (45) can be expressed as

$$u_{\text{IMC}} = (k_{pe} + k_{py})x_1 + (k_{ie1} + k_{iy1})x_2 + (k_{ie2} + k_{iy2})x_3 + k_{ie3}x_4. \quad (49)$$

The mathematical model of the current loop can then be written as

$$L\dot{i}(t) = u_{\text{IMC}} - Ri. \quad (50)$$

By combining (48) and (49) and using the fact  $\dot{i}_{\text{ref}} = 0$ , we can find that

$$\begin{aligned} \dot{x}_1 = & -1/L[(k_{pe} + k_{py} + R)x_1 + (k_{ie1} + k_{iy1}) \\ & x_2 + (k_{ie2} + k_{iy2})x_3 + k_{ie3}x_4]. \end{aligned} \quad (51)$$

Then, the state space equation of the Robust-IMC can be represented as follows:

$$\dot{x} = Ax \quad (52)$$

where  $x = [x_4, x_3, x_2, x_1]^T$ , and  $A \in \mathfrak{R}^4$  is a constant matrix. The elements of  $A$  are zero except  $A(4, 1) = -k_{ie3}/L$ ,  $A(4, 2) = -(k_{ie2} + k_{iy2})/L$ ,  $A(4, 3) = -(k_{ie2} + k_{iy2})/L$ ,  $A(4, 4) = -(k_{pe} + k_{py} + R)/L$ , and  $A(1, 2) = A(2, 3) = A(3, 4) = 1$ .

It is not difficult to verify that the dynamic model in (52) is stable if  $A$  is a Hurwitz matrix, and the current error  $e(t)$  will converge to zero in a finite time.

### E. Design of the FOVR-Robust-IMC

According to the analysis in Sections III-B–III-D, the FOVR-Robust-IMC is proposed in this study. The proposed controller incorporates both FOVR and Robust-IMC, which can provide satisfactory performances in harmonics suppression and robustness with respect to model mismatching and uncertain disturbances. The diagram of the

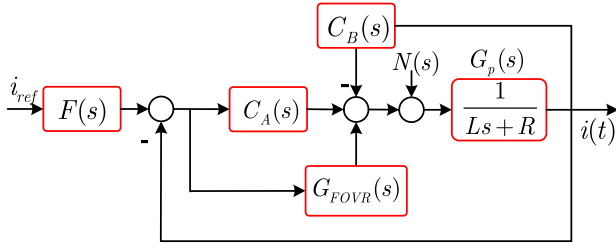


Fig. 7. Diagram of the FOVR-Robust-IMC controller.

FOVR-Robust-IMC is shown in Fig. 7, and the closed-loop transfer function is expressed as

$$i(s) = \frac{[C_A(s) + G_{\text{FOVR}}(s)]G_p(s)F(s)}{1 + (C_A(s) + G_{\text{FOVR}}(s) + C_B(s))G_p(s)} i_{\text{ref}}(s) + \frac{G_p(s)}{1 + (C_A(s) + G_{\text{FOVR}}(s) + C_B(s))G_p(s)} N(s) \quad (53)$$

where  $i(s)$  and  $i_{\text{ref}}(s)$  denote the transfer functions of  $i(t)$  and  $i_{\text{ref}}(t)$  in the  $s$ -domain.

The fractional-order term  $s^\alpha$  in  $G_{\text{FOVR}}(s)$  will bring several fractional-order poles and zeros [37]. Hence,  $G_{\text{FOVR}}(s)$  can be rewritten as

$$G_{\text{FOVR}}(s) = 2k_r\omega_c \prod_{i=1}^n G_{Ri}(s) \quad (54)$$

where  $G_{Ri}(s)$  is a transfer function containing a zero and a pole (i.e.,  $(s + z_i)/(s + p_i)$ ). The poles and zeros in  $G_{\text{FOVR}}(s)$  are calculated by Outstaloup's approximation method [37], except

$$z_1 = -R/L, \quad p_1 = -\omega_c + \sqrt{\omega_c^2 - (6\omega_h)^2}, \\ p_2 = -\omega_c - \sqrt{\omega_c^2 - (6\omega_h)^2}.$$

To analyze the stability and robust stability of the proposed FOVR-Robust-IMC, the conditions and their proofs are detailed in this section.

**Theorem 1 (Stability):** The proposed FOVR-Robust-IMC is stable if the following condition is satisfied:

$$\left\| \prod_{i=1}^n G_{Ri}(s) \right\|_\infty < \left\| \frac{1 + G_p(s)(C_A(s) + C_B(s))}{2k_r\omega_c G_p(s)} \right\|_\infty \quad (55)$$

where  $\|\cdot\|_\infty$  denotes the infinite norm. Then, the FOVR-Robust-IMC is asymptotically stable.

*Proof:* According to (53) and (54), the characteristic polynomial of the current loop is expressed as follows:

$$L(s) = [1 + G_p(s)(C_A(s) + C_B(s))] \times \left[ 1 + \frac{2k_r\omega_c G_p(s) \prod_{i=1}^n G_{Ri}(s)}{1 + G_p(s)(C_A(s) + C_B(s))} \right]. \quad (56)$$

Assume that the constant matrix  $A$  represented in III-D is Hurwitz, and then,  $C_A(s)$  and  $C_B(s)$  can yield  $1 + G_p(s)(C_A(s) + C_B(s))$  stable; i.e., the roots of  $1 + G_p(s)(C_A(s) + C_B(s))$  are located in the stability domain of the  $s$ -plane. Thus, the stability with the proposed FOVR-Robust-IMC is only affected by the following transfer function:

$$\Theta(s) = \frac{2k_r\omega_c G_p(s) \prod_{i=1}^n G_{Ri}(s)}{1 + G_p(s)(C_A(s) + C_B(s))}. \quad (57)$$

Based on the small-gain theorem [38], the stability condition for the proposed controller can be represented as

$$\left\| \frac{2k_r\omega_c G_p(s) \prod_{i=1}^n G_{Ri}(s)}{1 + G_p(s)(C_A(s) + C_B(s))} \right\|_\infty \leq \left\| \frac{2k_r\omega_c G_p(s)}{1 + G_p(s)(C_A(s) + C_B(s))} \right\|_\infty \left\| \prod_{i=1}^n G_{Ri}(s) \right\|_\infty < 1. \quad (58)$$

According to (57) and (58), (55) can be derived. The proof is complete.

**Theorem 2 (Robust Stability):** The control plant can be denoted as  $\tilde{G}_p(s) = G_p(s)(1 + \Delta G_p(s))$  considering model parameter mismatch and uncertainty.  $\Delta G_p(s)$  is the model error.

Assume that the control plant  $G_p(s)$  can be stabilized by  $C_A(s)$ ,  $C_B(s)$ , and  $G_{\text{FOVR}}(s)$ , i.e., (55) is satisfied. Thus, the current loop is robust stability if the following condition is fulfilled:

$$\|\Delta G_p(s)\|_\infty < \left\| \frac{1}{L(s) - 1} \right\|_\infty. \quad (59)$$

*Proof:* The characteristic polynomial with  $\tilde{G}_p(s)$  is represented as (60), shown at the bottom of the page, where  $Q(s) = (G_p(s)(C_A(s) + 2k_r\omega_c \prod_{i=1}^n G_{Ri}(s) + C_B(s)) / (1 + G_p(s)(C_A(s) + 2k_r\omega_c \prod_{i=1}^n G_{Ri}(s) + C_B(s))))$ .

According to (55), the stability of  $L(s)$  can be ensured. Consequently, to guarantee the robust stability of the current loop,  $(1 + Q(s)\Delta G_p(s))$  should be stable. Based on the small gain theorem presented in [38], a sufficient condition for robust stability can be obtained as follows:

$$\|Q(s)\Delta G_p(s)\|_\infty \leq \|Q(s)\|_\infty \|\Delta G_p(s)\|_\infty < 1. \quad (61)$$

$$\begin{aligned} \tilde{L}(s) &= 1 + G_p(s)(1 + \Delta G_p(s)) \times (C_A(s) + 2k_r\omega_c \prod_{i=1}^n G_{Ri}(s) + C_B(s)) \\ &= [1 + G_p(s)(C_A(s) + 2k_r\omega_c \prod_{i=1}^n G_{Ri}(s) + C_B(s))] \\ &\quad \times \left[ 1 + \frac{G_p(s)(C_A(s) + 2k_r\omega_c \prod_{i=1}^n G_{Ri}(s) + C_B(s))}{1 + G_p(s)(C_A(s) + 2k_r\omega_c \prod_{i=1}^n G_{Ri}(s) + C_B(s))} \Delta G_p(s) \right] \\ &= L(s)(1 + Q(s)\Delta G_p(s)) \end{aligned} \quad (60)$$

TABLE I  
 PARAMETERS OF THE PMSM

Symbol	Quantity	Value
L	d-q frame inductance	0.0085 H
R	Armature resistance	0.569 $\Omega$
P	Number of pole pairs	3
f	Flux linkage	0.035 Wb
J	Inertia	0.0012 kg·m <sup>2</sup>
T <sub>R</sub>	Rated torque	10 N·m
S <sub>R</sub>	Rated speed	250 r/min
I <sub>R</sub>	Rated current	7A

 TABLE II  
 PARAMETERS OF THE FOVR-ROBUST-IMC

$\lambda$	$\tau$	$L_n$	$R_n$	$k_r$	$\omega_c$	$\alpha$
0.0006	0.002	0.0085	0.569	1	10	1.2

It imposes that

$$\begin{aligned} & \left\| \frac{1}{\Delta G_p(s)} \right\|_{\infty} \\ & < \left\| 1 + \frac{1}{G_p(s)(C_A(s) + 2k_r\omega_c \prod_{i=1}^n G_{Ri}(s) + C_B(s))} \right\|_{\infty} \\ & < \left\| \frac{1}{G_p(s)(C_A(s) + 2k_r\omega_c \prod_{i=1}^n G_{Ri}(s) + C_B(s))} \right\|_{\infty}. \quad (62) \end{aligned}$$

According to (62), the robust stability condition presented in (59) can be deduced.

#### IV. SIMULATION AND EXPERIMENTAL VERIFICATION

Simulations and experiments are carried out to verify the performance of the proposed controller. Table I presents the parameters of the PMSM, and Table II gives the parameters of FOVR-Robust-IMC.

##### A. Simulation Results

The simulation is performed in MATLAB-Simulink. The switching frequency of the inverter is 10 kHz, and the voltage of the dc link is 300 V. The PMSM is an ideal model, and torque ripples caused by current harmonics will not appear in the simulation. To simulate an actual motor drive system, the sixth-harmonic component is injected into the inverter. The overall Simulink control diagram based on the FOVR-Robust-IMC is shown in Fig. 8. Two simulations are conducted to validate the proposed FOVR-Robust-IMC. These simulations focus on the current dynamic response with parameters' mismatch and current harmonics suppression performance.

##### a) Current Loop Robustness to Parameters' Mismatch:

In order to equitably evaluate the robustness of the control strategies, the PI and FOVR-Robust-IMC are tuned to enable the dynamic response to achieve a transient process with a preset settling time (in this article,  $\tau$  is set as 0.002), and the

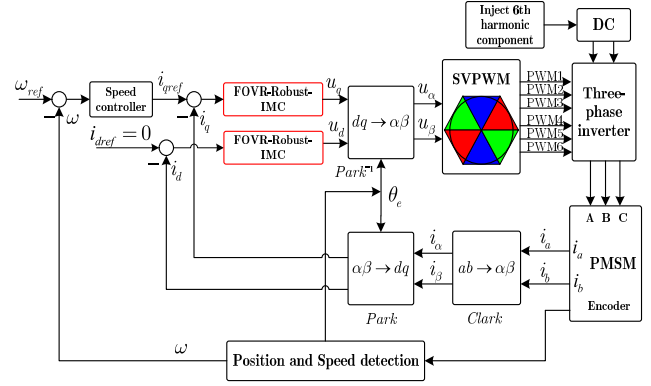
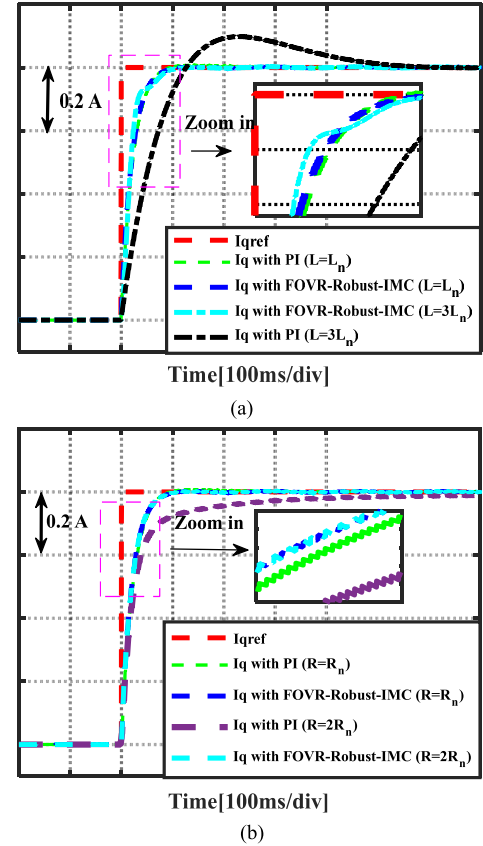


Fig. 8. Structure diagram of the proposed FOVR-Robust-IMC.


 Fig. 9. Current loop dynamic response with a parameter mismatch. (a) Inductance mismatch with  $L = 3L_n$ . (b) Resistance mismatch with  $R = 2R_n$ .

parameters of the PI controller are set as  $k_{pd} = k_{pq} = \tau^{-1}L_n$  and  $k_{id} = k_{iq} = \tau^{-1}R_n$  (where  $k_{pd}$  and  $k_{pq}$  are the proportional gains;  $k_{id}$  and  $k_{iq}$  are the integral gains). The original tracking trajectory will be set as a reference. The robustness testing simulations are then performed in the current loop with parameter mismatching. Note that the parameters of the PI and FOVR-Robust-IMC remain fixed; thus, the tracking performance is only affected by the variation parameters of the control plant.

Fig. 9(a) shows the step tracking when an inductance mismatch occurs under  $L = 3L_n$ . It can be observed in

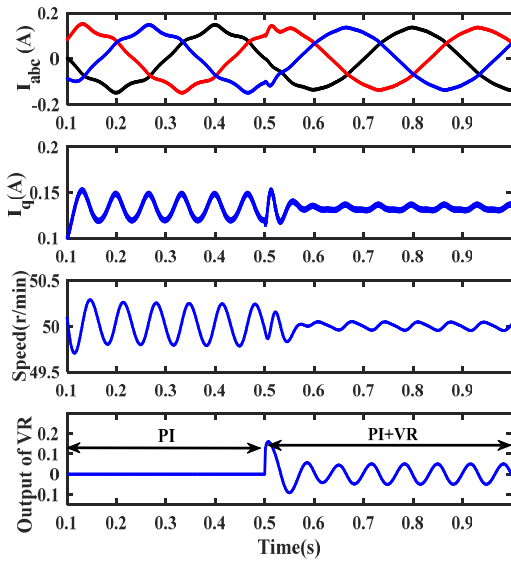


Fig. 10. Steady-state performance of the PI and PI-VR controllers at the speed of 50 rpm.

the tracking trajectory (dark trace) of the PI controller that a large overshoot appears, and a long settling time required to reach the current command of 0.8 A is shown. However, the FOVR-Robust-IMC can still provide a satisfactory dynamic response with a rapid dynamic response without overshoot (sky blue trace).

Fig. 9(b) demonstrates the dynamic response when resistance mismatches  $R = 2R_n$ . It can be observed that the actual current of the PI controller requires a long settling time to reach the steady state (violet trace). Moreover, a large steady-state error occurs in the tracking trajectory. However, the transition process and steady state of the FOVR-Robust-IMC (sky blue trace) shows minimal change after parameter variation. These simulation results prove that the proposed FOVR-Robust-IMC is robust to parameter mismatching.

*b) Current Harmonics Suppression Performance Evaluation in a Steady State:* To verify the correctness of the proposed controller, the current controller is a pure PI or Robust-IMC at 0–0.5 s. At 0.5 s, the VR or FOVR controller is enabled and employed in the current loop. These simulations test at low and high speeds of 50 and 200 rpm, respectively, to focus on the current and speed of the steady-state performance.

Figs. 10–12 show the steady-state performance under different control methods with a speed command  $\omega_m$  of 50 rpm. When the speed command is set to  $\omega_m$ , the corresponding electrical angular velocity is  $\omega_h = 2\pi p\omega_m/60$ . Thus, the center frequency of the FOVR controller can be determined.

It can be observed from Fig. 10 that the phase current shows some distortion with the fifth and seventh harmonics when the PI control method is used independently. The fast Fourier transform (FFT) analysis using MATLAB shows that the total harmonic distortion (THD) in the three-phase current reaches 6.75%. The steady-state error for the  $q$ -axis current fluctuates with sixth harmonics. The speed loop ripple also

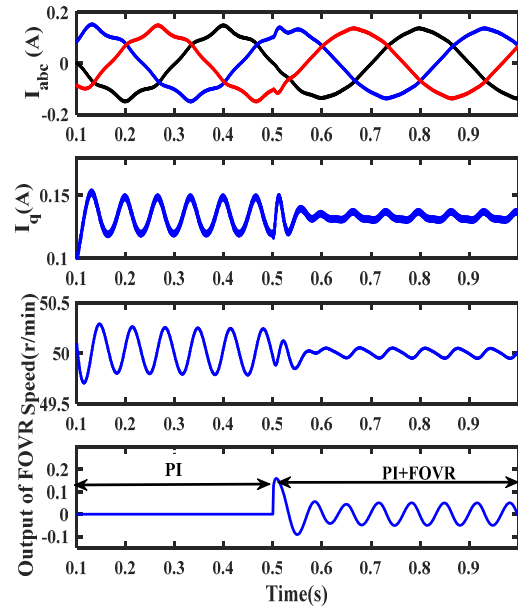


Fig. 11. Steady-state performance of PI and PI-FOVR controllers at the speed of 50 rpm.

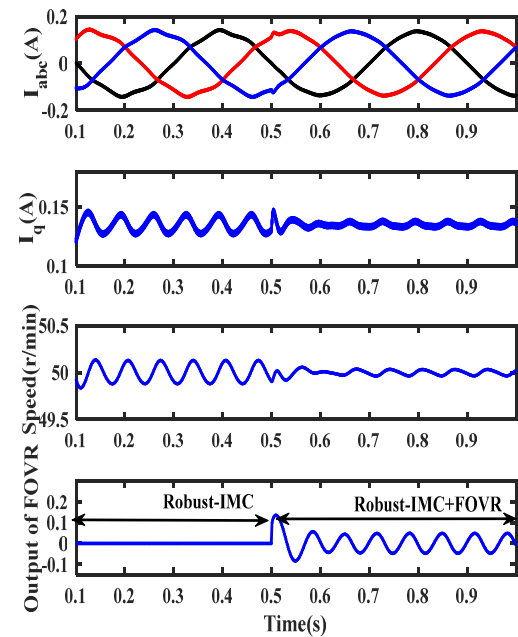


Fig. 12. Steady-state performance of the Robust-IMC and FOVR-Robust-IMC controllers at the speed of 50 rpm.

shows sixth harmonics with the amplitude of 0.25 rpm. The VR controller is enabled for the current loop at 0.5 s. It is evident that the VR controller output is a sixth-harmonic component that can compensate for the phase current with fifth and seventh harmonics. Meanwhile, the amplitude of the sixth harmonics in the speed loop is reduced to 0.053 rpm. However, the phase current  $I_{abc}$  after compensation still shows some distortion with a THD of 1.78%.

Fig. 11 illustrates the steady-state performance of the PI-FOVR controller. The THD calculated by FFT is reduced to 1.65%. In addition, the speed ripple is decreased to 0.049 rpm.

TABLE III  
SIMULATION RESULTS UNDER THE OPERATION OF LOW SPEED

	PI control	PI-VR control	PI-FOVR control	Robust-IMC control	FOVR-Robust-IMC control
THD (%)	6.75	1.78	1.65	3.98	0.85
Speed tracking error (r/min)	0.25	0.053	0.049	0.14	0.031

TABLE IV  
SIMULATION RESULTS UNDER THE OPERATION OF HIGH SPEED

	PI control	PI-VR control	PI-FOVR control	Robust-IMC control	FOVR-Robust-IMC control
THD (%)	8.03	2.12	1.98	4.23	1.02
Speed tracking error (r/min)	0.26	0.0498	0.0487	0.11	0.02

The steady-state error of the  $q$ -axis current is also effectively eliminated. By comparing the steady-state behavior of the PI-VR controller and the PI-FOVR controller, we find that the PI-FOVR controller can further reduce the  $q$ -axis current and speed steady-state error caused by current harmonics.

Fig. 12 demonstrates steady-state performance with the pure Robust-IMC controller (0–0.5 s) and the proposed FOVR-Robust-IMC controller (0.5–1 s). When the  $q$ -axis current is independently regulated with Robust-IMC, the phase current has a THD of 3.98%, and the sixth harmonics with an amplitude of 0.14 rpm occurs in the speed. Although the current harmonics with Robust-IMC is decreased by 41% compared with the PI controller, the harmonic component is still large. When the FOVR-Robust-IMC is utilized in the current loop, the THD is decreased to 0.85%, and the steady-state error of the  $q$ -axis current is also effectively eliminated. The steady-state speed error remains at 0.031 rpm. These results suggest that the proposed controller can achieve satisfactory current harmonics suppression at low speeds. The simulation results under the low-speed operation are shown in Table III.

Figs. 13–15 show the steady-state performance of the above controllers at a high speed (200 rpm). When the PI controller is employed independently, the phase current has a THD of 8.03%, and the speed ripple with sixth harmonics was 0.26 rpm. As shown in Table IV, after the VR and FOVR controllers are each enabled, the THD percentage of phase current harmonics are reduced to 2.12% and 1.98%, and the speed ripples decrease to 0.0498 and 0.0487 rpm, respectively. By comparing the steady-state performances between the

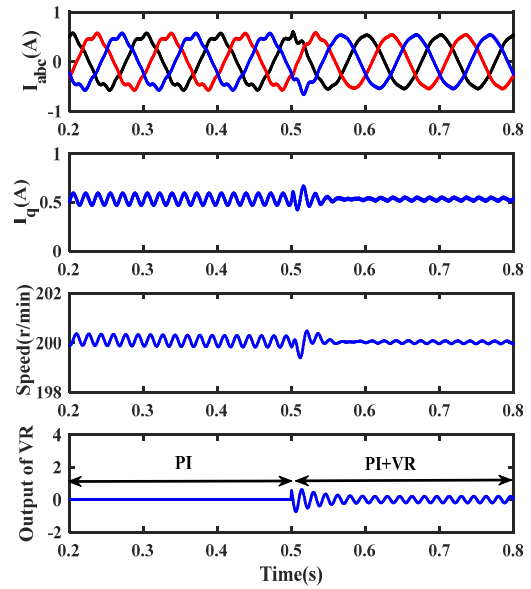


Fig. 13. Steady-state performance of the PI and PI-VR controllers at the speed of 200 rpm.

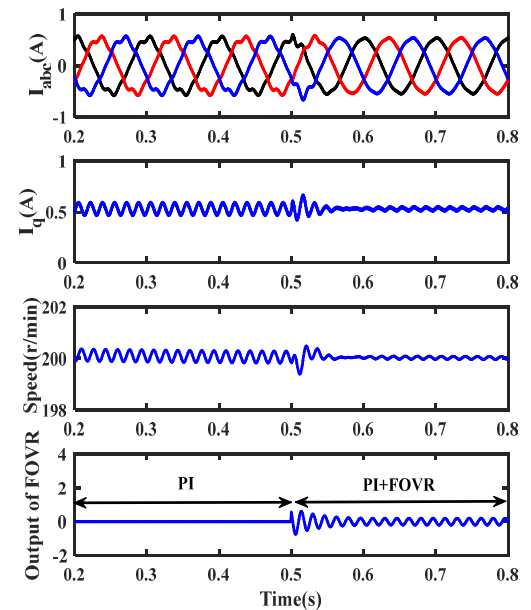


Fig. 14. Steady-state performance of the PI and PI-FOVR controllers at the speed of 200 rpm.

VR and FOVR controllers, we find that the FOVR controller has better harmonics suppression performance. Furthermore, when the Robust-IMC is utilized in the current loop, the THD is 4.23%, and the speed steady-state error is 0.11 rpm. By comparing the simulation results with those of the PI controller, it is clearly observed that the Robust-IMC is more suitable as the auxiliary controller than the PI controller. After the FOVR controller is enabled in the current loop, the THD is further decreased to 1.02%, and the speed steady-state error is maintained at 0.02 rpm. According to the above analysis, it can be observed the combination of FOVR and Robust-IMC provides better harmonics suppression performance than PI,

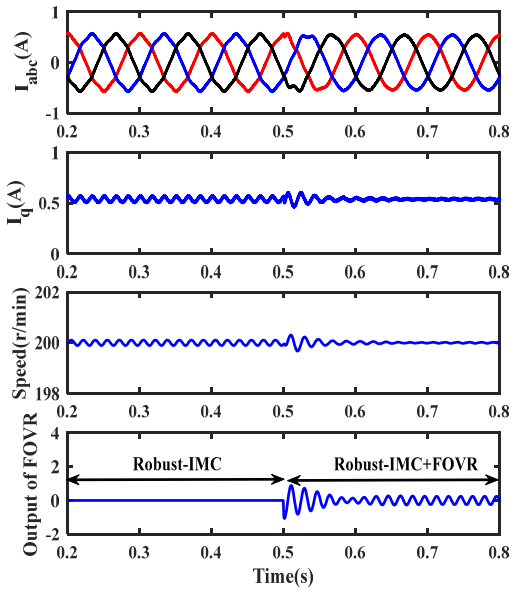


Fig. 15. Steady-state performance of the Robust-IMC and FOVR-Robust-IMC controllers at the speed of 200 rpm.

PI-VR, PI-FOVR, and pure Robust-IMC control methods under the operation of high speeds. The simulation results are listed in Tables III and IV.

*c) Current Harmonics Suppression Performance Evaluation During the Transition Period:* The harmonics suppression performance evaluation of our control method during the transition period is conducted. When the motor runs in the steady state, a sudden load with the value of 0.5 N.m acts on the motor at 5 s. The data from the transition period of 5–5.4 s are used to analyze the THD values. It can be observed in Fig. 16 that the PI-FOVR controller improves the current quality, and the torque ripple is decreased. When the FOVR-Robust-IMC controller is used, the current quality is further enhanced. The THDs of PI, PI-FOVR, and FOVR-Robust-IMC are 10.16%, 6.85%, and 5.72%, respectively. The simulation demonstrates that the FOVR-Robust-IMC can maintain better performance in torque ripple minimization during the transition period compared to the PI and PI-FOVR methods.

Fig. 17 shows the current waveforms with parameter mismatching. It is determined that the current distortion with PI and PI-FOVR is further distorted. The THDs with the two control methods are 10.78% and 12.93%, respectively. By contrast, the THD of our method is only 5.97%. It is apparent that the proposed FOVR-Robust-IMC controller can guarantee better harmonics suppression performance under the condition of parameter mismatching.

## B. Experimental Results

The proposed FOVR-Robust-IMC is tested on the drive setup of a TMS320F28335 digital signal processor (DSP) and EP3C40F324 field-programmable gate array (FPGA). Fig. 18 illustrates the overall experimental platform of the PMSM system, and a photograph of the experimental platform is shown in Fig. 19. The experimental motor adopts a

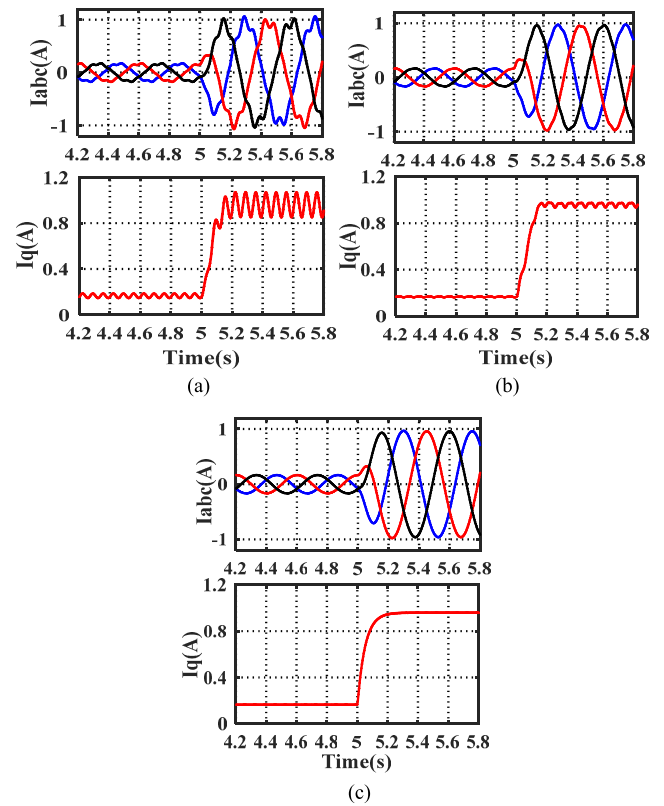


Fig. 16. Phase current and  $q$ -axis current waveforms under the sudden load condition. (a) With the PI controller. (b) With the PI-FOVR controller. (c) With our method.

surface-mounted structure (delta-connected stator windings). Table I lists the motor parameters. An FPGA is used for A/D conversion, encoder reading, speed detection, and generation of insulated-gate bipolar transistor gate-switching signals. The DSP is a 32-bit floating-point microcontroller to ensure fast computation. The sampling frequencies of the velocity and current loops are 1 and 10 kHz, respectively. The experiments are performed to validate the effectiveness of the proposed FOVR-Robust-IMC.

*1) Current Dynamic Behavior Evaluation:* In this experiment, the current command value  $i_{qref}$  is changed from 0 to 0.6 A, and the  $d$ -axis current is maintained at 0 A. Fig. 20 depicts the results of the step response of the  $d$ - $q$ -axis current under the PI and FOVR-Robust-IMC control algorithms. Fig. 20(a) shows the current response of the PI controller. It is clearly observed that overshooting occurs in the transition process, which results in a large settling time required to reach the steady state. Fig. 20(b) demonstrates the current dynamic response with FOVR-Robust-IMC. It is observed that the FOVR-Robust-IMC can ensure a faster dynamic response to reach the steady state. Second, the overshoot is obviously less compared to that of the PI controller. Therefore, the control method of using FOVR-Robust-IMC can guarantee a faster tracking speed in the transition process.

Note that the actual inductance and resistance parameters of a motor cannot be changed randomly. Therefore, the robust test experiment is performed by changing the parameters of the FOVR-Robust-IMC. Fig. 20(c) shows the dynamic response

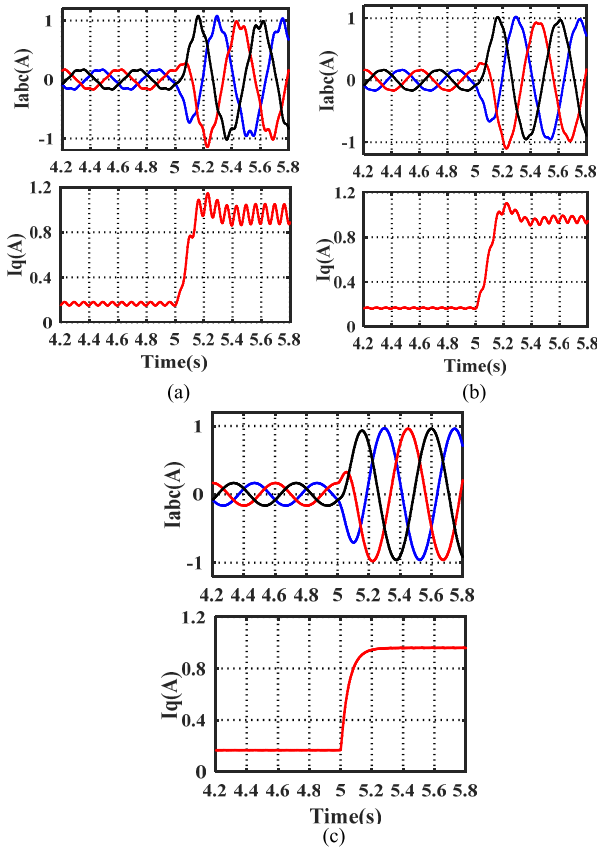


Fig. 17. Phase current and  $q$ -axis current waveforms under the sudden load condition with a parameter mismatch of  $L = 3L_n$  and  $R = 2R_n$ . (a) With the PI controller. (b) With the PI-FOVR controller. (c) With our method.

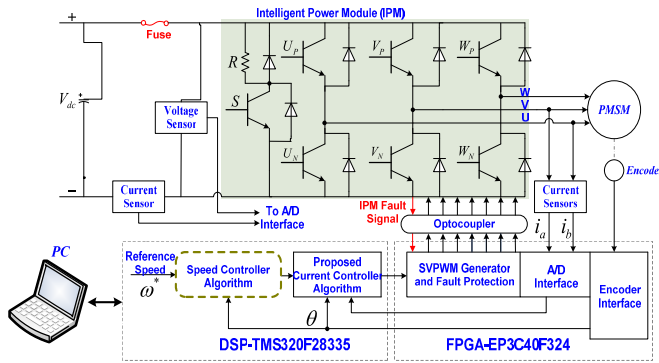


Fig. 18. Structural diagram of the PMSM servo system.

with the proposed controller when parameters' mismatch ( $L = 3L_n$ ,  $R = 2R_n$ ). It is evident that the proposed controller can still provide the desired transition process with only a small overshoot and a fast dynamic response in such a case. Hence, we can conclude that the proposed FOVR-Robust-IMC has strong robustness to parameter mismatching.

*d) Harmonics Suppression Performance Evaluation of the Proposed Controller:* Experiments are conducted to adequately validate the effectiveness of the FOVR-Robust-IMC method in terms of harmonics attenuation under low- and high-speed conditions. The pure PI controller is applied to obtain the original torque ripple situation of the PMSM control



Fig. 19. Photograph of the experimental platform.

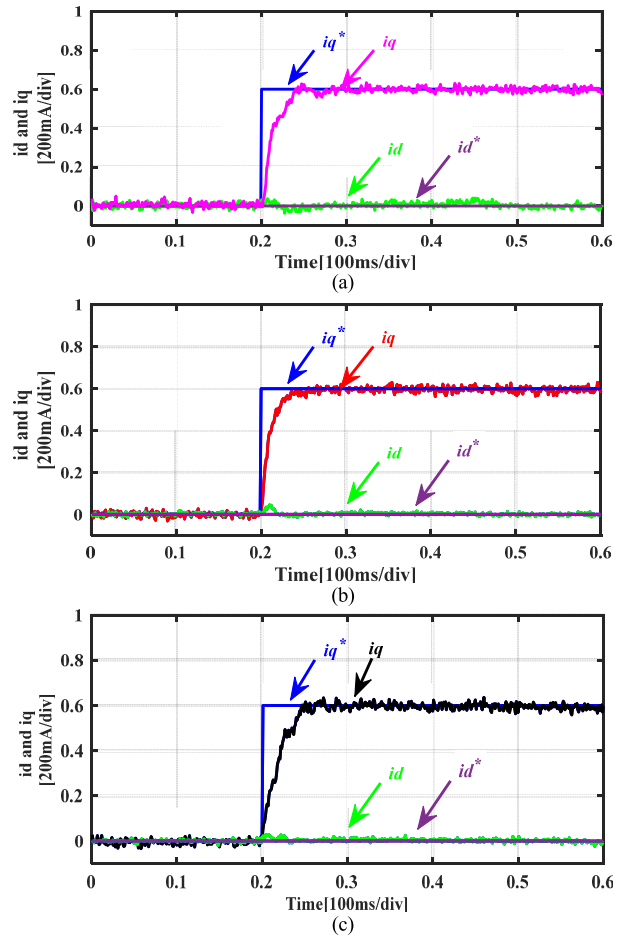


Fig. 20. Experimental results at step signal of  $i_{qref}$  with amplitude from 0 to 6 A. (a) Current step response with the PI controller. (b) Current step response with FOVR-Robust-IMC. (c) Current step response with FOVR-Robust-IMC controller when parameter mismatch  $L = 3L_n$ ,  $R = 2R_n$ .

system without compensation. The VR controller and the proposed FOVR controller are enabled at 6 s. In order to evaluate the result of the proposed method at minimizing torque ripples, the ratio of the average actual speed to the speed command is used as an index of the steady-state speed tracking performance, i.e.,  $SRF = S_{as}/S_{cs}$ . The THD of the phase current  $I_a$  is employed to evaluate the current distortion caused by harmonics.

Fig. 21 shows the actual steady-state behavior of the PMSM without and with the VR controller at a low speed (50 rpm). The quality of the current waveform  $I_a$  is deteriorated by the fifth- and seventh-order harmonics at 5.6–6 s.  $I_a$  without

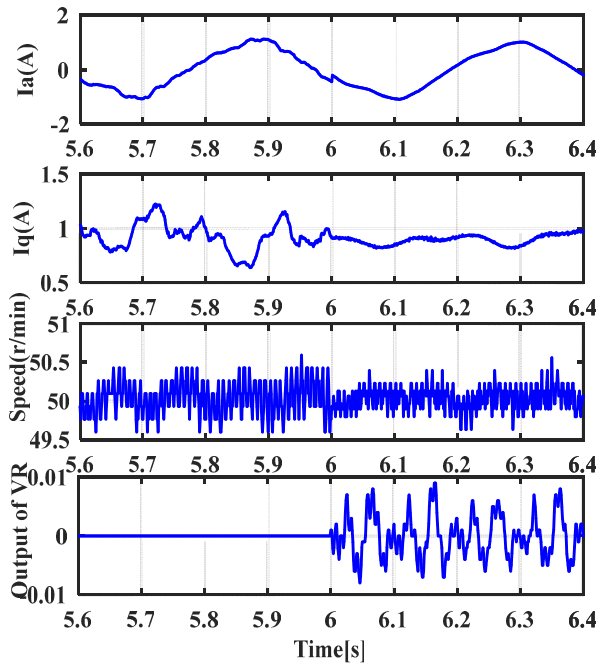


Fig. 21. Experimental results for the steady-state performance with PI and PI-VR controllers at a speed command of 50 rpm.

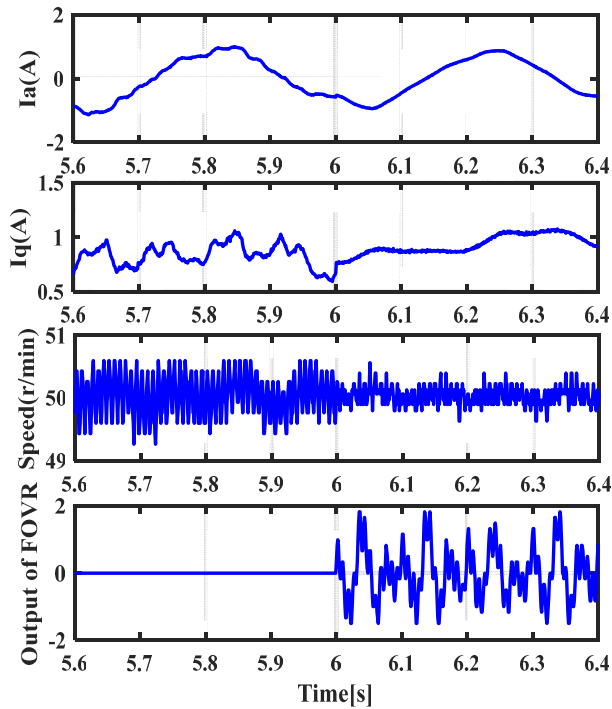


Fig. 22. Experimental results for the steady-state performance with the PI and PI-FOVR controllers at a speed command of 50 rpm.

compensation of the VR controller has a THD of 8.23%. Meanwhile, the current  $I_q$  and speed tracking show some fluctuation. The SRF is 1.64% for this speed. When the VR controller is enabled at 6 s,  $I_a$ ,  $I_q$ , and speed tracking are notably improved. The THD decreases by 68.89%, from 8.23% to 2.56%. In addition, the SRF decreases to 1.52%.

As can be observed from Fig. 22, the FOVR controller can further reduce the distortions of the phase currents  $I_a$

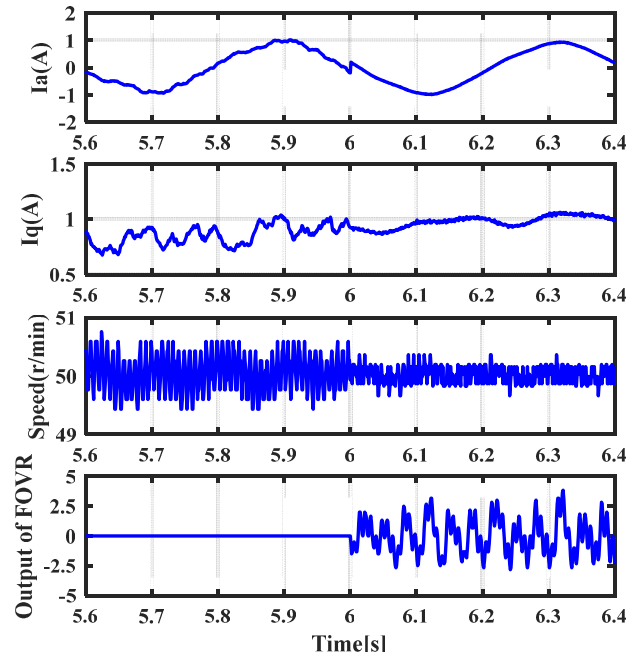


Fig. 23. Experimental results for the steady-state performance with the Robust-IMC and FOVR-Robust-IMC at a speed command of 50 rpm.

and  $I_q$ . With the FOVR controller, the THD reduces to 2.17%, and the corresponding SRF decreases to 1.47%. These results show that the FOVR controller can provide better harmonic suppression than the pure PI control strategy and the VR controller at low speeds.

Fig. 23 depicts the steady-state performance of the pure Robust-IMC and FOVR-Robust-IMC. When the Robust-IMC controller is used alone, the THD and SRF are 6.83% and 1.61%, respectively. After the FOVR controller is enabled at 5.6 s, the THD and SRF decrease to 1.86% and 1.42%, respectively. These experimental results demonstrate that the proposed FOVR-Robust-IMC can provide better harmonics suppressing performance than the other controllers mentioned in this article under the low-speed operation.

Figs. 24–26 show the actual performance at a speed command of 200 rpm. According to Fig. 24, the THD and SRF of the PI control method are 10.84% and 3.35%, respectively. When the VR controller is enabled, the THD and SRF reduce to 3.61% and 3.12%. Fig. 25 shows the experimental results for the PI-FOVR controller. For the phase current and speed, the THD and SRF become 2.26% and 3.05%, respectively. These results show that the FOVR controller effectively suppresses harmonics at high speeds. It is evident in Fig. 26 that the THDs of the pure Robust-IMC and the proposed FOVR-Robust-IMC are 8.96% and 1.76%, and the corresponding SRFs are 3.18% and 2.55%, respectively.

According to the experimental analysis, it is clearly observed that the FOVR-Robust-IMC can maintain satisfactory harmonics suppression at low and high speeds. Tables V and VI present the experimental results under different operation conditions.

e) *Current Harmonics Suppression Performance Evaluation During the Transition Period:* Fig. 27 presents the experimental results of the harmonics suppression performance

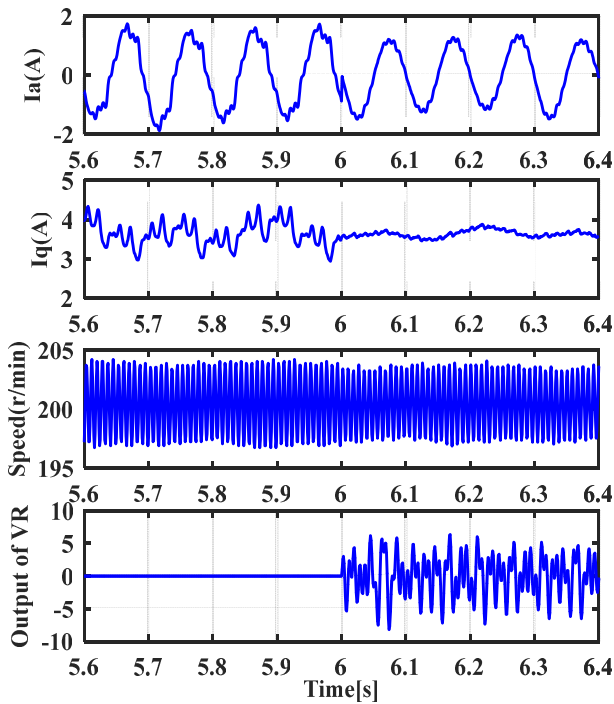


Fig. 24. Experimental results for the steady-state performance with PI and PI-VR controllers at a speed command of 200 rpm.

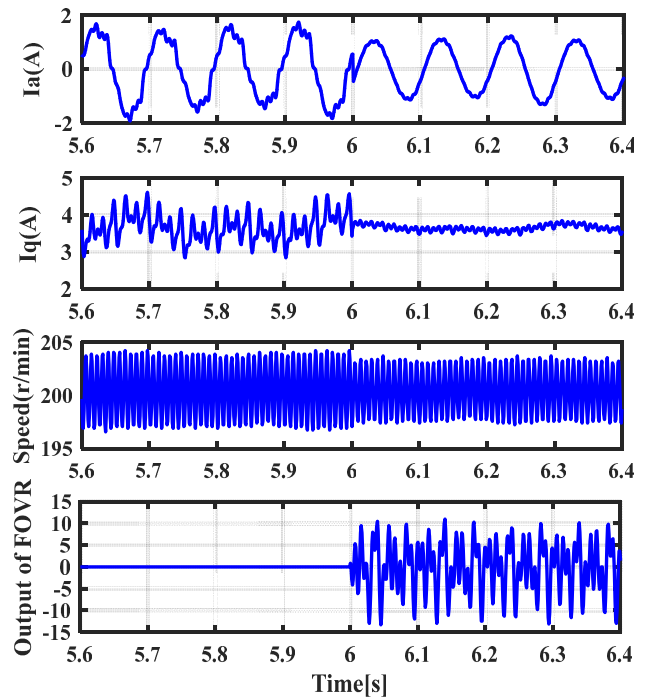


Fig. 26. Experimental results for the steady-state performance with the Robust-IMC and FOVR-Robust-IMC at a speed command of 200 rpm.

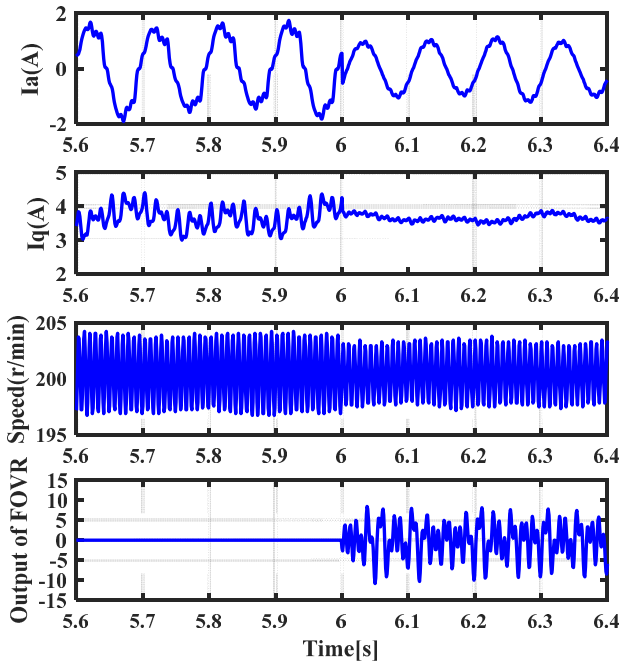


Fig. 25. Experimental results for the steady-state performance with the PI and PI-FOVR controller at a speed command of 200 rpm.

during the transition period. Fig. 27(a) shows the phase current  $I_a$  and  $q$ -axis current with the PI controller. It can be observed that a large ripple occurs in the currents, and the THD of  $I_a$  is 11.86%. As can be seen from Fig. 27(b), the current quality is improved when PI-FOVR controller is used in current loop, and the THD value is decreased to 8.41%. Fig. 27(c) depicts the current waveforms with the proposed FOVR-Robust-IMC.

TABLE V

EXPERIMENTAL RESULTS UNDER THE OPERATION OF LOW SPEED

	PI control	PI-VR control	PI-FOVR control	Robust-IMC control	FOVR-Robust-IMC control
THD (%)	8.23	2.56	2.17	6.83	1.86
SRF (%)	1.64	1.52	1.47	1.61	1.42

TABLE VI

EXPERIMENTAL RESULTS UNDER THE OPERATION OF HIGH SPEED

	PI control	PI-VR control	PI-FOVR control	Robust-IMC control	FOVR-Robust-IMC control
THD (%)	10.84	3.61	2.26	8.96	1.76
SRF (%)	3.35	3.12	3.05	3.18	2.55

It is apparent that the currents are further enhanced, and the THD is decreased to 6.85%. The harmonics suppression performance of our method during the period with parameters' mismatch of  $L = 3L_n$  and  $R = 2R_n$  is shown in Fig. 27(d). It can be seen that the currents quality is decreased in some degree compared with FOVR-Robust-IMC ( $L = L_n$  and  $R = R_n$ ), and the corresponding THD is 7.22%. However, it still performs better harmonics suppression performance than PI and PI-FOVR controllers. The experimental results show that the proposed controller can guarantee satisfactory harmonics suppression performance during the transition period although the parameters of the motors change.

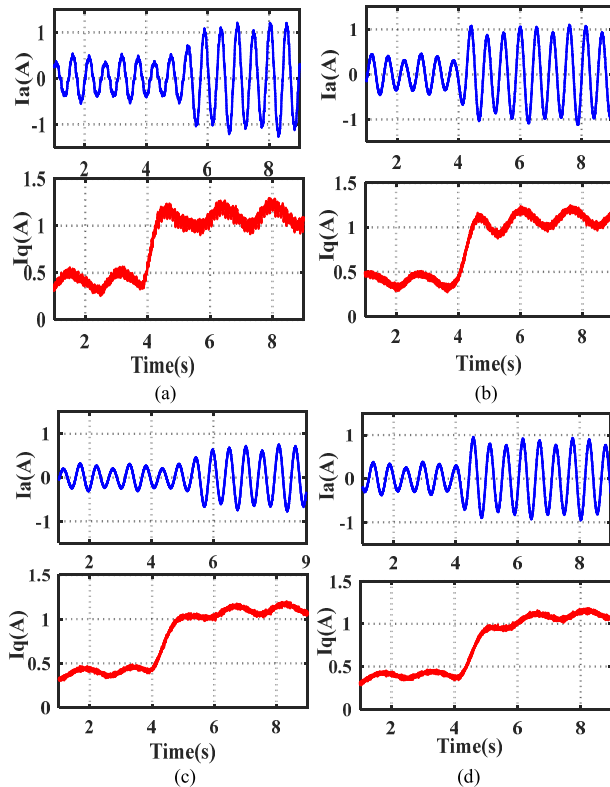


Fig. 27. Experimental results of phase current and  $q$ -axis current waveforms under the sudden load condition. (a) With the PI controller. (b) With the PI-FOVR controller. (c) Our method with the parameter of  $L = L_n$  and  $R = R_n$ . (d) Our method with a parameter mismatch of  $L = 3L_n$  and  $R = 2R_n$ .

## V. CONCLUSION

In this study, a novel FOVR-Robust-IMC was developed by combining a designed FOVR controller and Robust-IMC. Compared to the VR controller, the designed FOVR controller provides a larger phase margin while maintaining a higher gain, which can further minimize the steady-state error caused by current harmonics. The Robust-IMC is designed to achieve robustness with respect to parameter mismatching and to obtain the desired tracking trajectory. The multicondition simulation and experimental results showed that the proposed FOVR-Robust-IMC provides better harmonics suppression than the PI, Robust-IMC, PIR, and PI-FOVR controllers. The main contributions of this article are as follows.

- 1) A review of resonant controllers is given, followed by the details of the FOVR controller designed in this study. The proposed FOVR controller is shown to improve harmonics suppression performance compared to the VR controller.
- 2) Based on a combination of the proposed FOVR controller and the Robust-IMC, a new FOVR-Robust-IMC control strategy is developed to suppress the current harmonics, improve the robustness to parameter mismatching, and obtain the desired dynamic response. The distinct properties of stability and robust stability are analyzed based on the small gain theorem.
- 3) The harmonics suppression and robustness performance of the proposed FOVR-Robust-IMC are verified through simulations and experiments.

## REFERENCES

- [1] F. Betin *et al.*, "Trends in electrical machines control: Samples for classical, sensorless, and fault-tolerant techniques," *IEEE Ind. Electron. Mag.*, vol. 8, no. 2, pp. 43–55, Jun. 2014.
- [2] Q. Fei, Y. Deng, H. Li, J. Liu, and M. Shao, "Speed ripple minimization of permanent magnet synchronous motor based on model predictive and iterative learning controls," *IEEE Access*, vol. 7, pp. 31791–31800, 2019.
- [3] L. Jarzebowicz, "Errors of a linear current approximation in high-speed PMSM drives," *IEEE Trans. Power Electron.*, vol. 32, no. 11, pp. 8254–8257, Nov. 2017.
- [4] Z. Zhang, X. Ge, Z. Tian, X. Zhang, Q. Tang, and X. Feng, "A PWM for minimum current harmonic distortion in metro traction PMSM with saliency ratio and load angle constrains," *IEEE Trans. Power Electron.*, vol. 33, no. 5, pp. 4498–4511, May 2018.
- [5] C. Jiu Jian, M. Wen Li, and H. Jin Long, "Design and optimization of arc permanent magnet synchronous motor used on large telescope," *IEEE Trans. Magn.*, vol. 48, no. 5, pp. 1943–1947, May 2012.
- [6] C. Zhu, Z. Zeng, and R. Zhao, "Comprehensive analysis and reduction of torque ripples in three-phase four-switch inverter-fed PMSM drives using space vector pulse-width modulation," *IEEE Trans. Power Electron.*, vol. 32, no. 7, pp. 5411–5424, Jul. 2017, doi: 10.1109/TPEL.2016.2605160.
- [7] K. Liu and Z. Q. Zhu, "Position offset-based parameter estimation for permanent magnet synchronous machines under variable speed control," *IEEE Trans. Power Electron.*, vol. 30, no. 6, pp. 3438–3446, Jun. 2015.
- [8] C. Lai, G. Feng, K. Mukherjee, V. Loukanov, and N. C. Kar, "Torque ripple modeling and minimization for interior PMSM considering magnetic saturation," *IEEE Trans. Power Electron.*, vol. 33, no. 3, pp. 2417–2429, Mar. 2018.
- [9] J. Liu, H. Li, and Y. Deng, "Torque ripple minimization of PMSM based on robust ILC via adaptive sliding mode control," *IEEE Trans. Power Electron.*, vol. 33, no. 4, pp. 3655–3671, Apr. 2018.
- [10] N. Nakao and K. Akatsu, "Suppressing pulsating torques: Torque ripple control for synchronous motors," *IEEE Ind. Appl. Mag.*, vol. 20, no. 6, pp. 33–44, Nov. 2014.
- [11] K.-C. Kim, "A novel method for minimization of cogging torque and torque ripple for interior permanent magnet synchronous motor," *IEEE Trans. Magn.*, vol. 50, no. 2, pp. 793–796, Feb. 2014.
- [12] W. Fei and P. C.-K. Luk, "Torque ripple reduction of a direct-drive permanent-magnet synchronous machine by material-efficient axial pole pairing," *IEEE Trans. Ind. Electron.*, vol. 59, no. 6, pp. 2601–2611, Jun. 2012.
- [13] W. Qian, S. K. Panda, and J.-X. Xu, "Torque ripple minimization in PM synchronous motors using iterative learning control," *IEEE Trans. Power Electron.*, vol. 19, no. 2, pp. 272–279, Mar. 2004.
- [14] P. Mattavelli, L. Tubiana, and M. Zigliotto, "Torque-ripple reduction in PM synchronous motor drives using repetitive current control," *IEEE Trans. Power Electron.*, vol. 20, no. 6, pp. 1423–1431, Nov. 2005.
- [15] P. Cui, S. Li, G. Zhao, and C. Peng, "Suppression of harmonic current in active-passive magnetically suspended CMG using improved repetitive controller," *IEEE/ASME Trans. Mechatronics*, vol. 21, no. 4, pp. 2132–2141, Aug. 2016.
- [16] T. Liu and D. Wang, "Parallel structure fractional repetitive control for PWM inverters," *IEEE Trans. Ind. Electron.*, vol. 62, no. 8, pp. 5045–5054, Aug. 2015.
- [17] M. Wu, L. Zhou, and J. She, "Design of observer-based  $H_\infty$  robust repetitive-control system," *IEEE Trans. Autom. Control*, vol. 56, no. 6, pp. 1452–1457, Jun. 2011.
- [18] Y. Yan, J. Yang, Z. Sun, C. Zhang, S. Li, and H. Yu, "Robust speed regulation for PMSM servo system with multiple sources of disturbances via an augmented disturbance observer," *IEEE/ASME Trans. Mechatronics*, vol. 23, no. 2, pp. 769–780, Apr. 2018.
- [19] B. Xie *et al.*, "Analysis and improved design of phase compensated proportional resonant controllers for grid-connected inverters in weak grid," *IEEE Trans. Energy Convers.*, vol. 35, no. 3, pp. 1453–1464, Sep. 2020.
- [20] O. Husev, C. Roncero-Clemente, E. Makovenko, S. P. Pimentel, D. Vinnikov, and J. Martins, "Optimization and implementation of the proportional-resonant controller for grid-connected inverter with significant computation delay," *IEEE Trans. Ind. Electron.*, vol. 67, no. 2, pp. 1201–1211, Feb. 2020.
- [21] Z. Zhou, C. Xia, Y. Yan, Z. Wang, and T. Shi, "Disturbances attenuation of permanent magnet synchronous motor drives using cascaded predictive-integral-resonant controllers," *IEEE Trans. Power Electron.*, vol. 33, no. 2, pp. 1514–1527, Feb. 2018.

- [22] M. Elkayam, S. Kolesnik, and A. Kuperman, "Guidelines to classical frequency-domain disturbance observer redesign for enhanced rejection of periodic uncertainties and disturbances," *IEEE Trans. Power Electron.*, vol. 34, no. 4, pp. 3986–3995, Apr. 2019.
- [23] A. G. Yepes, F. D. Freijedo, Ó. Lopez, and J. Doval-Gandoy, "High-performance digital resonant controllers implemented with two integrators," *IEEE Trans. Power Electron.*, vol. 26, no. 2, pp. 563–576, Feb. 2011.
- [24] Y. Chen, I. Petras, and D. Xue, "Fractional order control—A tutorial," in *Proc. Amer. Control Conf.*, Jul. 2009, pp. 1397–1411.
- [25] I. Pan and S. Das, "Chaotic multi-objective optimization based design of fractional order  $PI^2D^\mu$  controller in AVR system," *Int. J. Electr. Power Energy Syst.*, vol. 43, no. 1, pp. 393–407, Dec. 2012.
- [26] W. Zhen and Y. Pi, "Study of the fractional order proportional integral controller for the permanent magnet synchronous motor based on the differential evolution algorithm," *ISA Trans.*, vol. 63, pp. 387–393, Jul. 2016.
- [27] D. Pullaguram, S. Mishra, N. Senroy, and M. Mukherjee, "Design and tuning of robust fractional order controller for autonomous microgrid VSC system," *IEEE Trans. Ind. Appl.*, vol. 54, no. 1, pp. 91–101, Jan. 2018.
- [28] C. Xia, B. Ji, and Y. Yan, "Smooth speed control for low-speed high-torque permanent-magnet synchronous motor using proportional-integral-resonant controller," *IEEE Trans. Ind. Electron.*, vol. 62, no. 4, pp. 2123–2134, Apr. 2015.
- [29] C. Liu, F. Blaabjerg, W. Chen, and D. Xu, "Stator current harmonic control with resonant controller for doubly fed induction generator," *IEEE Trans. Power Electron.*, vol. 27, no. 7, pp. 3207–3220, Jul. 2012.
- [30] Y. Deng, J. Wang, H. Li, J. Liu, and D. Tian, "Adaptive sliding mode current control with sliding mode disturbance observer for PMSM drives," *ISA Trans.*, vol. 88, pp. 113–126, May 2019.
- [31] Y. Ik Son, I. Hyuk Kim, D. Sik Choi, and H. Shim, "Robust cascade control of electric motor drives using dual reduced-order PI observer," *IEEE Trans. Ind. Electron.*, vol. 62, no. 6, pp. 3672–3682, Jun. 2015.
- [32] C. Xia, B. Ji, T. Shi, and Y. Yan, "Two-degree-of-freedom proportional integral speed control of electrical drives with Kalman-filter-based speed estimation," *IET Electr. Power Appl.*, vol. 10, no. 1, pp. 18–24, Jan. 2016.
- [33] R. Teodorescu, F. Blaabjerg, M. Liserre, and P. C. Loh, "Proportional resonant controllers and filters for grid-connected voltage-source converters," *IEEE Proc. Electr. Power Appl.*, vol. 153, no. 5, pp. 750–762, Sep. 2006.
- [34] G. Franklin, J.D. Powell, and A. Emami-Naeini, *Feedback Control of Dynamic Systems*, 5th ed. Englewood Cliffs, NJ, USA: Prentice-Hall, 2006.
- [35] P. Li and G. Zhu, "Robust internal model control of servo motor based on sliding mode control approach," *ISA Trans.*, vol. 93, pp. 199–208, Oct. 2019.
- [36] F. Mendoza-Mondragon, V. M. Hernandez-Guzman, and J. Rodriguez-Resendiz, "Robust speed control of permanent magnet synchronous motors using two-degrees-of-freedom control," *IEEE Trans. Ind. Electron.*, vol. 65, no. 8, pp. 6099–6108, Aug. 2018.
- [37] W. Jakowluk, "Fractional-order linear systems modeling in time and frequency domains," in *Computer Information Systems and Industrial Management*, K. Saeed, W. Homenda, R. Chaki, Eds. Cham, Switzerland: Springer, 2017, pp. 502–513.
- [38] C. A. Desoer and M. Vidyasagar, *Feedback Systems: Input-Output Properties*. New York, NY, USA: Academic, 1975.



**Mingfei Huang** was born in Chongqing, China, in 1993. He received the B.E. degree from Hainan University, Haikou, China, in 2017. He is currently pursuing the Ph.D. degree with the University of Chinese Academy of Sciences, Beijing, China, and the Changchun Institute of Optics, Fine Mechanics and Physics, Chinese Academy of Sciences, Changchun, China.

His research interests include ac motor drive and control design, fractional-order control, and digital control using digital signal processor (DSP).



**Yongting Deng** (Member, IEEE) was born in Shandong, China, in 1987. He received the B.E. degree from the China University of Petroleum, Beijing, China, and the M.S. and Ph.D. degrees from the Changchun Institute of Optics, Fine Mechanics and Physics, Chinese Academy of Sciences, Changchun, China, in 2015.

He is currently an Associate Professor with the Changchun Institute of Optics, Fine Mechanics and Physics, Chinese Academy of Sciences. His research interests include controller design for ac motor

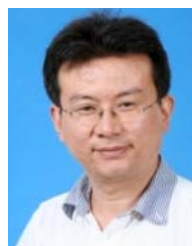
drives and linear motor drives, intelligent control, and digital control implemented with digital signal processor (DSP) and field-programmable gate array (FPGA).



**Hongwen Li** (Member, IEEE) was born in Sichuan, China, in 1970. He received the M.S. degree from the Jilin University of Technology, Changchun, China, in 1996, and the Ph.D. degree from Jilin University, Changchun, in 2007.

From 1996 to 2002, he was an Associate Professor with the Jilin University of Technology. Since 2002, he has been with the Changchun Institute of Optics, Fine Mechanics, and Physics, Chinese Academy of Sciences, Changchun, where he is currently a Professor with the Department of Optical-Electronic

Detection. His research interests include optical–electric sensor technologies, switching-mode power supply techniques, electric machines and drives, and high-precision machine control techniques. He has authored/coauthored more than 50 publications in these areas.



**Jianli Wang** (Member, IEEE) was born in Shandong, China, in 1971. He received the Ph.D. degree from the Changchun Institute of Optics, Fine Mechanics and Physics, Chinese Academy of Sciences, Changchun, China, in 2002.

He is currently a Professor with the Changchun Institute of Optics, Fine Mechanics and Physics, Chinese Academy of Sciences. His research interests include optical–electric telescope, high-resolution imaging, and high-precision machine control techniques. He has authored/coauthored more than 100 publications in these areas.